Forecasting Convective Initiation by Monitoring the Evolution of Moving Cumulus in Daytime GOES Imagery

John R. Mecikalski

Atmospheric Science Department, University of Alabama in Huntsville, Huntsville, Alabama

Kristopher M. Bedka

Cooperative Institute for Meteorological Satellite Studies, Space Science and Engineering Center, University of Wisconsin—Madison, Madison, Wisconsin

ABSTRACT

This study identifies the precursor signals of convective initiation within sequences of 1-km-resolution visible (VIS) and 4–8-km infrared (IR) imagery from the Geostationary Operational Environmental Satellite (GOES) instrument. Convective initiation (CI) is defined for this study as the first detection of Weather Surveillance Radar-1988 Doppler (WSR-88D) reflectivities $\geq$35 dBZ produced by convective clouds. Results indicate that CI may be forecasted ~30–45 min in advance through the monitoring of key IR fields for convective clouds. This is made possible by the coincident use of three components of GOES data: 1) a cumulus cloud "mask" at 1-km resolution using VIS and IR data, 2) satellite-derived atmospheric motion vectors (AMVs) for tracking individual cumulus clouds, and 3) IR brightness temperature (T_B) and multispectral band-differencing time trends. In effect, these techniques isolate only the cumulus convection in satellite imagery, track moving cumulus convection, and evaluate various IR cloud properties in time. Convective initiation is predicted by accumulating information within a satellite pixel that is attributed to the first occurrence of a $\geq$35 dBZ radar echo. Through the incorporation of satellite tracking of moving cumulus clouds, this work represents a significant advance in the use of routinely available GOES data for monitoring aspects of cumulus clouds important for nowcasting CI (0–1-h forecasts). Once cumulus cloud tracking is established, eight predictor fields based on Lagrangian trends in IR data are used to characterize cloud conditions consistent with CI. Cumulus cloud pixels for which $\geq$7 of the 8 CI indicators are satisfied are labeled as having high CI potential, assuming an extrapolation of past trends into the future. Comparison to future WSR-88D imagery then measures the method's predictive skill. Convective initiation predictability is demonstrated using several convective events—one during IHOP_2002—that occur over a variety of synoptic and mesoscale forcing regimes.

1. Introduction

As the resolution (in both space and time) of atmospheric observing systems increases, so does our ability to monitor and forecast aspects of mesoscale weather phenomena. One aspect that has gained increased interest is the short-term prediction of rainfall events, especially those that evolve on meso–time scales ($\leq$~3 h), which certainly include thunderstorm convection. Because thunderstorms are accompanied by rapidly changing weather on spatial and temporal scales important to travelers, energy providers, and aviation interests, and produce weather hazards and phenomena that often adversely impact professionals ranging from farmers to pilots, there is a critical need to accurately predict their development, evolution, and movement. In particular, hazards related to thunderstorms (lightning, hail, strong winds, and wind shear) cost the aviation industry many tens of millions of dollars annually in lost time, fuel, and efficiency through delayed, canceled, and rerouted flights, as well as accidents (Mecikalski et al. 2002; Murray 2002).

The International H$_2$O Project that took place in spring 2002 (IHOP_2002) had as one main objective to gain an improved understanding of the convective ini-

Corresponding author address: Prof. John R. Mecikalski, Atmospheric Science Department, University of Alabama in Huntsville, 320 Sparkman Drive, Huntsville, AL 35805-1912.
E-mail: john.mecikalski@nsstc.uah.edu

tiation (CI) process and subsequent thunderstorm development (Weckwerth et al. 2004). The initiation of rainfall in convective clouds is difficult to predict in part because of the highly nonlinear dynamic processes occurring on short time scales over which convection evolves (minutes to ~1 h), and the ubiquitous lack of observations of moisture and flow kinematics on scales of hundreds of meters to ~2 km that lead to upward mass transports of water vapor and temperature structures above the convective boundary layer (e.g., Mueller et al. 1993; Medlin and Croft 1998). Weckwerth (2006) provides an overview of the current state of knowledge of CI in the context of IHOP_2002.

The premises that guide this work are 1) the CI process is well observed by satellite as small cumulus clouds grow to the cumulonimbus scale, and 2) processing geostationary satellite data in near–real time is an optimal means of evaluating the evolving CI process. The purpose of this study then is to evaluate, in near–real time satellite imagery, the visible (VIS) and infrared (IR) signals of CI toward the development of a CI "nowcasting" (0–1-h forecasting) algorithm. In particular, processing daytime geostationary satellite imagery from the *Geostationary Operational Environmental Satellite-11* (*GOES-11*) and *-12* (*GOES-12*) instruments is done to identify cumulus clouds for which CI is likely to occur in the near future. The outcome is an evaluation of how sequences of VIS and IR data can be used to predict CI ~30–45 min prior to its occurrence during daytime hours. As VIS and IR data are processed, eight predictors for describing the character, growth, and evolution of convective clouds are identified, assuming cumulus clouds can be accurately tracked between images at intervals of 5–15 min. These predictors include IR cloud-top brightness temperatures (T_B's), IR multispectral channel differences, and IR cloud-top T_B/multispectral temporal trend assessments using satellite-derived atmospheric motion vectors (AMVs hereafter) for cloud tracking. All satellite-based parameters eventually found to be important for nowcasting CI are related to important dynamic and thermodynamic aspects of convective clouds undergoing the transition into organized rain-producing systems.

The definition for CI employed in this study is the first occurrence of rainfall with ~35 dBZ reflectivity as measured by operational, ground-based radar. This definition is appropriate given our research goal of identifying cumulus clouds likely to evolve into precipitating thunderstorms within the 0–1-h time frame. The 35-dBZ criterion was chosen because this level of rainfall intensity has been well correlated with the eventual development of mature cumulonimbus clouds (see Roberts and Rutledge 2003). The tracking of radar signatures of storms using satellite data has severe limitations, due to the poor relationship between the cloud motions viewed by satellite and rainfall detected by radar, and is thus not employed within this study.

The quality of these nowcasts is determined through direct comparison against "truth" provided by regional mosaics of Weather Surveillance Radar-1988 Doppler (WSR-88D) data for several case events across the United States and near-shore regions. When relying on the use of satellite cloud-motion AMVs to track cumulus, there is an awareness that these clouds may evolve significantly over the time intervals between successive images. As a result, several issues must be addressed when determining the accuracy of our methods. These include the difficulty matching satellite-observed cumulus convection to radar echoes, and the errors associated with tracking small cumulus (<3 km in horizontal scale) in 5–15-min resolution data, which can result in discrepancies between observed rainfall and cloud location. These issues are discussed in concert with the forthcoming analysis.

The satellite-based analysis of convective storms began with the Applications Technology Satellites (ATS) I–V from the mid-1960s to early 1970s, and continues with today's GOES instruments (*GOES-9–12* in particular), Advanced Very High Resolution Radiometer (AVHRR), Moderate Resolution Imaging Spectroradiometer (MODIS), Meteosat, and its second-generation instrument MSG. The newest geostationary instruments (i.e., *GOES-12* and MSG) possess 1-km-horizontal-resolution visible light sensors and 4–8-km-resolution IR sensors, both at high temporal resolution (5–15 min between images). The strength of geostationary satellite data as a forecasting tool for tropospheric weather phenomena, with time scales of ≤6 h and length scales in the meso-γ to meso-β (2–200 km) range, lies in the ability to view and track features in successive images.

The analysis and monitoring of convective weather from satellites has taken several general forms, which include the evaluation of IR convective cloud-top properties (e.g., Riehl and Schleusener 1962; McCann 1983; Hill 1991; Setvák and Doswell 1991; Strabala et al. 1994; Levizzani and Setvák 1996; Minnis and Young 2000; Setvák et al. 2003), and the identification of active updrafts using IR techniques (Adler and Fenn 1979; Ackerman 1996; Schmetz et al. 1997) coupled with other datasets such as lightning (Roohr and Vonder Haar 1994). The Setvák and Doswell (1991), Strabala et al. (1994), and Schmetz et al. (1997) methods link physical properties of cloud tops, in particular, the microphysi-

cal character, with IR temperature difference thresholds. Roberts and Rutledge (2003, RR03 hereafter) very recently developed methods that correlate satellite IR cloud-top temperature trends with radar reflectivity for quasi-stationary convection.

More advanced processing techniques include feature recognition, objective identification, and tracking of cumulus clouds. Studies by Hand (1996) and Nair et al. (1998, 1999) describe methods of feature identification and quantification using statistical classifiers. Pattern-analysis evaluation of cumulus and cumulonimbus anvils has a long history (Fujita et al. 1975; Adler and Fenn 1979; Adler et al. 1985), with more recent studies employing sophisticated image processing algorithms (Setvák et al. 2003) and convective cloud classification (e.g., Uddstrom and Gray 1996) using neural networks (Baum et al. 1997). Purdom (1976, 1982, 1986), Beckman (1986), and many similar studies presented within satellite imagery interpretation manuals (e.g., Parke 1986; Weldon and Holmes 1991) have adequately outlined what a forecaster must identify as the precursors of CI. Recent advances in satellite image processing have resulted in satellite-derived soundings (Schreiner et al. 2001) from which parameters such as lifted index, precipitable water, convective available potential energy (CAPE), and convective inhibition (CIN) can be estimated at 10-km resolution from the GOES sounder instrument (Hayden et al. 1996; Menzel et al. 1998; Schmit et al. 2002). These products are useful for determining the character of the convective environment (i.e., airmass boundaries, stability gradients).

Given the passive detection methods of meteorological satellites, considerable effort must be placed on discerning convection and isolating the signals of CI in these data. Broad weighting functions, overlapping clouds, effects of gaseous (i.e., water vapor and carbon dioxide) and aerosol absorption on IR temperatures and brightness counts in VIS data, surface reflectance and emissivity, and the poor correlation between clouds and ground-based radar-detected precipitation exemplify the problems associated with using satellite data for identifying convective storm development. Despite these deficiencies, when monitoring convection over large-scale regions, over oceans, or where radar (and other "active" sensors) is ineffective or not available, meteorological satellites offer a very effective tool.

This paper proceeds as follows. Section 2 details the data, research methods, and processing techniques, while section 3 presents several case study examples demonstrating the performance of these techniques in nowcasting CI. Analysis errors and uncertainties are addressed in section 4, and the paper is summarized and concluded in section 5.

2. Technique development

Summarizing the literature, previous efforts utilizing satellite imagery for evaluating CI and convective storm evolution have taken several forms: 1) VIS/IR cloud pattern analysis, 2) IR single- and multispectral channel analyses, and 3) time trend analysis of IR T_B/multispectral differencing. These three analysis methods are *combined* in this study to produce CI nowcasts for several diverse convective events. Therefore, the new work presented here, in many ways, builds on particularly relevant past research.

For this study, the GOES Imager 4–8-km resolution IR data are interpolated to the 1-km VIS resolution. By doing this, the IR analysis techniques can be directly combined with the VIS data in ways that preserve the high detail and value the VIS data provide to the CI nowcast problem. Data from the GOES sounder are not utilized due to its coarse temporal (every hour) and spatial resolution (10 km).

Each field developed from the VIS and IR data is referred to as an "interest field." Certainly, not all CI interest fields provide the same level of information (value) to a CI nowcast, as will be explained below (see Table 1). The following discussion describes each interest field and its contribution to the CI nowcast algorithm (Table 2).

a. Convective cloud mask

IR-based interest fields are computed only where convective clouds are present, thereby excluding approximately 70%–90% (on average) of a given satellite image. This has the obvious benefit of greatly increasing processing speed, allowing for real-time (CI) assessments over large geographical domains. A combination of four techniques are used to identify convective clouds in *GOES-11* and *-12* imagery: 1) brightness gradient evaluation for preliminary identification of "immature," nonprecipitating cumulus (i.e., cumulus sans anvil or glaciation), 2) brightness thresholding for preliminary identification of "mature" cumulus, which are likely precipitating (i.e., glaciated, assuming non-"warm top" convection where ice nucleation is not involved in initiating precipitation), 3) 10.7-μm T_B time-differencing thresholds to separate immature cumulus that meet the brightness threshold criterion yet are improperly classified as mature, and 4) a textural analysis of VIS brightness values to separate low, thick stratus clouds from the mature cumulus classification. Figure 1 provides a flowchart demonstrating the processing for the convective cloud mask. Image processing done prior to forming the cumulus mask consists of correcting for bad scan lines, performing "noise" reduction,

TABLE 1. The information the *GOES-12* satellite can provide to the CI nowcast algorithm, and their individual contributions in terms of uniqueness for assessing CI. For GOES satellites prior to *GOES-12*, similar statements can be made when comparing 6.7- vs 6.5-μm and 12.0- vs 13.3-μm channels.

GOES-12 derived field	Contribution	Uniqueness
Visible brightness counts	Convective cloud mask	Unique
10.7-μm T_B	Convective cloud mask and cloud-top temperature assessment	Unique
3.9-, 6.5-, 13.3-μm T_B		Redundant
3.9–10.7-μm difference	Cloud-top microphysical assessment (not used due to effect of solar zenith angle on 3.9-μm band)	Not used
6.5–10.7-μm difference	Cloud-top height relative to tropopause	Unique
13.3–10.7-μm difference	Cloud-top height changes	Unique
10.7-μm temporal trend	Cloud-top cooling rates	Unique
3.9-, 6.5-, 13.3-μm temporal trend		Redundant
3.9–10.7-μm temporal trend	Time changes in cloud-top microphysics	Not used
6.5–10.7-μm temporal trend	Time changes in cloud height relative to the tropopause	Unique
13.3–10.7-μm temporal trend	Time changes in cloud-top height	Unique
Visible and infrared winds	Cumulus cloud tracking for temporal trend assessment	Unique

and enhancing cloud edges using a shot noise filter within the Man-computer Interactive Data Access System (McIDAS; provided by the "IMGFILT" command).

A unique attribute of cumulus clouds in the sharpened imagery is their high brightness (in terms of visible brightness counts), and thus their distinct edges relative to noncloudy regions. To locate cumulus cloud edges, horizontal gradients of brightness counts are computed. These gradients are calculated in four directions: north–south, east–west, northeast–southwest, and northwest–southeast. Horizontal gradients larger than ~60 brightness counts per 2 km have been determined to indicate the presence of a cumulus cloud edge, where a transition from a dark, cloud-free pixel to a bright, cumulus cloud pixel occurs. This technique only identifies cumulus cloud edges, thereby giving nonprecipitating cumulus of horizontal scales greater than ~5 km a "ringlike" appearance. This problem is rectified by also classifying pixels in the middle of these rings as cumulus.

The next step identifies mature cumulus and their associated cirrus anvils using a brightness thresholding technique. In most cases, cumulus clouds are the brightest of all features in VIS satellite imagery due to their microphysical composition of small, supercooled water droplets/ice crystals and high optical thickness in the visible wavelengths (Wielicki and Welch 1986). We utilize this attribute to identify clouds with brightness counts greater than a defined time-of-day-, time-of-year-dependent brightness threshold, which varies from approximately 160 (out of 255) at solar noon near the winter solstice to 180 near the summer solstice. We set this threshold quite high in order to identify cumulonimbus and thick cirrus anvil clouds. Unfortunately, the brightness threshold technique occasionally misclassi-

fies immature cumulus and thick stratus clouds as mature cumulus near solar noon when the maximum amount of solar radiation is reflected. Therefore, several additional quality-control checks are invoked to address this problem.

The -20°C 10.7-μm T_B (IR) threshold, described by RR03, is subsequently used to separate immature from mature cumulus and cirrus. In essence, it is assumed that cumulus that meet the brightness threshold criterion have IR temperatures $>-20^\circ$C, and have not begun to precipitate, are still immature.

TABLE 2. A summary of the per-pixel criteria used in the CI nowcast algorithm for the imager instruments on the *GOES-11* (explicitly noted) and *GOES-12* satellites. A total of eight "scores" are given for each pixel in conjunction with each CI interest field. A given pixel must meet ≥ 7 of the 8 criteria to be identified as a cumulus with a high probability (~60%–70%) of evolving into a precipitating convective storm in the following 30–45-min time period.

CI interest field	Critical value
10.7-μm T_B (one score)	$<0^\circ$C
10.7-μm T_B time trend (two scores)	$<-4^\circ$C (15 min)$^{-1}$ ΔT_B (30 min)$^{-1} < \Delta T_B$ (15 min)$^{-1}$
Timing of 10.7-μm T_B drop below 0°C (one score)	Within prior 30 min
6.5 (or 6.7)–10.7-μm difference (one score)	-35° to -10°C
13.3–10.7-μm difference (one score)	-25° to -5°C
12.0–10.7-μm difference	-3° to 0°C (*GOES-11*)
6.5 (or 6.7)–10.7-μm time trend (one score)	$>3^\circ$ (15 min)$^{-1}$
13.3–10.7-μm time trend (one score)	$>3^\circ$ (15 min)$^{-1}$
12.0–10.7-μm time trend	$>2^\circ$ (5 min)$^{-1}$ (*GOES-11*)

Ingest GOES Visible Imagery from
Data Stream at UW-CIMSS

Apply Shot Noise Filter to Remove
Noise and Sharpen Cloud Edges

Use "Brightness Gradient" Technique to
identify immature cumulus

Use "Brightness Threshold" Technique
to identify mature cumulus

10.7 um and 6.5 (6.7) –10.7 µm
Checks to Identify Bright
Immature Cumulus

10.7 µm T_B > -20 ºC
6.5 (6.7) – 10.7 µm < -10 ºC
Likely Immature Cu

10.7 µm T_B < -20 ºC
6.5 (6.7) – 10.7 µm > -10 ºC
Likely Mature Cu

Visible Standard Deviation
Check for Cloud Texture

Warm Clouds (> -20 º C)
with High Texture:
Immature Cumulus

Warm Clouds (> -20 ºC)
with Little Texture:
Thick Stratus/Thin Cirrus

Cold Clouds (< -20 ºC)
with Little Texture:
Thick Cirrus

Cold Clouds (< -20 ºC)
with High Texture:
Mature Cumulus

FIG. 1. Flowchart demonstrating the necessary steps for producing the convective cloud mask.

Studies related to the identification of cloud patterns and cloud types through pattern analysis include those by Kuo et al. (1993), Bankert (1994), and Nair et al. (1998, 1999). In particular, Nair et al. (1999) utilizes both a structural thresholding method and classifiers based on the textural, statistical, and edge characteristics of cumulus clouds as seen in GOES 1-km visible band imagery. The standard deviation of brightness counts, calculated over a 5×5 pixel box centered at each previously classified cumulus cloud, is a final test toward separating highly reflective stratus clouds from mature cumulus. Another unique aspect of cumulus clouds in the VIS satellite is their "lumpy" appearance. Statistically, this "lumpiness" can be quantified by high standard deviations in brightness within the 5×5 pixel box. Clouds with high standard deviations retain their cumulus classification. Clouds with low standard deviations of brightness, 10.7-μm $T_B < -20°C$, and 6.5 (or 6.7)–10.7-μm differences $> -10°C$ (to be described in the following section) are denoted as cirrus clouds. Other pixels previously identified as mature cumulus

with low brightness standard deviations and 10.7-μm $T_B > -20°C$ are removed from the cumulus mask being that they likely represent highly reflective stratus clouds.

A summary of the IR predictor fields used to characterize cloud conditions consistent with CI is presented in Tables 2 and 3. These fields are described in detail below.

b. Channel differencing

The *GOES-11* (used for the IHOP_2002 event analyzed below) and *GOES-12* imager instruments detect radiation emitted by the earth surface/atmosphere within four IR spectral channels (bands) centered at 3.9 μm, 6.5 μm (6.7 μm for *GOES-11*), 10.7 μm, and 13.3 μm (12.0 μm for *GOES-11*), in addition to VIS light imagery (brightness 0–255; Menzel and Purdom 1994). Radiances are converted into T_B's, which are utilized to infer atmospheric and cloud properties. The maximum horizontal resolution (at nadir) of these IR channels ranges from 4 (for the 3.9-, 6.5-, 10.7-, and 12.0-μm

TABLE 3. *GOES* (*-11* and before, and *-12*) (left column) IR channel difference techniques and purpose and (right column) studies that demonstrate the method. Bottom two methods are used within this study to assess CI and thunderstorm development (of a $\geq$35 dBZ echo) as moving cumulus clouds are monitored for these interest fields. Note that because radiances from the 3.9-μm channel contain both emissive IR and reflected solar radiation components, values resulting from the 3.9–10.7-μm difference vary throughout the day as the solar zenith angle changes, making it difficult to establish difference thresholds for use in CI nowcasting. As a result, the 3.9–10.7-μm differencing is not used in this study.

Infrared method and purpose	Developer and demonstration
3.9–10.7-μm T_B's (cloud-top microphysics; *nighttime only*)	Ellrod (1995)
6.5 or 6.7–10.7-μm T_B's (cloud height relative to tropopause; cloud growth)	Ackerman (1996); Schmetz et al. (1997)
12.0/13.3–10.7-μm T_B's (cloud type; cloud-top height)	Inoue (1987); Prata (1989); Ellrod (2004)

bands) to 8 km (for the 6.7- and 13.3-μm bands). Table 1 describes how these "broadband" radiance channels may be used alone to assess convective cloud characteristics (e.g., 10.7 μm for cloud-top temperature in an "atmospheric window"), or two-channel differences may be developed toward measuring various cloud-top properties.

Infrared multispectral channel differencing is used here to identify cumulus in a pre-CI state. An analysis comparing IR channel differences to WSR-88D radar base reflectivity was performed for convection during ~seven case events (not presented in this study; *the dependent dataset*) to identify the difference values present before immature cumulus clouds evolved into rain-producing convective storms. From this analysis, IR band-difference relationships for cumulus prior to CI were formed. These values are subsequently used as CI interest fields within the nowcast algorithm and are tested on the cases described in section 3 (*the independent dataset*). These band-differencing techniques, and the critical values chosen for CI evaluation, are described below.

The 6.5/6.7–10.7-μm difference is useful for determining the cloud-top height relative to the tropopause, or to very dry mid- and upper-tropospheric air. Positive values of the water vapor–IR window temperature difference have been shown to correspond with convective cloud tops that are at or above the tropopause (i.e., overshooting tops), or growing into dry upper-tropospheric air where the water vapor band "saturates" near the same altitude of the 10.7-μm temperature (Ackerman 1996; Schmetz et al. 1997). In clear-sky situations, radiation at 6.5–6.7 μm is emitted by atmospheric water vapor between approximately 20 and 50 kPa (Soden and Bretherton 1993). The radiation emitted at 6.5–6.7 μm by the surface or low clouds is absorbed by atmospheric water vapor in the lower troposphere and is not detected by satellites. On the other hand, absorption by atmospheric gases at 10.7 μm is weak, and, therefore, detected radiation at 10.7 μm originates mainly from the surface. Because the surface is normally warmer than the upper troposphere, the difference between the 6.5–6.7- and 10.7-μm T_B is usually negative. In regions of intense convective updrafts, with cloud tops possibly extending into the lower stratosphere, the 10.7-μm T_B is colder than that at 6.5 μm, resulting in a positive T_B difference between these bands. For the assessment of pre-CI signatures, convective clouds with positive differences have likely already begun to precipitate, especially in tropical atmospheres that support warm-top convection. Therefore, clouds with moderately negative difference values (−35 to −10 K) represent a useful CI interest field and imply the presence of low- to midlevel cloud tops (~85–50 kPa).

The 12.0–10.7-μm differencing, known as the "split window" technique, can be used to identify the presence of cirrus, volcanic ash, and deep convective clouds in *GOES-11* imagery. The magnitude of this technique is dependent on the cloud optical thickness, the cloud liquid water and chemical constituent content (i.e., sulfur dioxide in volcanic ash clouds), and the size distribution of the particles in a cloud (Prata 1989). Satellite-detected thin cirrus cloud T_B's differ at these two wavelengths, resulting from the detection of (warm) emission of terrestrial radiation through a thin cloud layer at 10.7 μm. Clouds that are optically opaque such as cumulus or thick stratus clouds have nearly the same T_B at these two spectral bands. By subtracting these T_B's, regions of high, thin cirrus are identified by negative difference values (<−5 K; Strabala et al. 1994). Mature cumulus clouds with upper-tropospheric cloud tops exhibit slightly positive difference values, similar to the 6.5/6.7–10.7-μm technique described above. Inoue (1987) found near-zero 12–11-μm differences provide an improved identification of convective rainfall regions in comparison to conventional rainfall estimation algorithms that are based exclusively on using the <−20°C 10.7-μm T_B threshold (Griffith et al. 1978). Cumulus clouds in a pre-CI state exhibit difference values ranging from −3° to 0°C within the events of the dependent dataset.

The 13.3–10.7-μm difference is another measure used to characterize and delineate cumulus clouds in a pre-CI state from mature precipitating cumulus and cirrus in *GOES-12* imagery. Limited documentation of this band-difference method is available (Ellrod 2004), and therefore this study may be the first organized use of this technique for convective cloud studies (T. Schmit, NOAA, 2003, personal communication). The subtraction of the 10.7 μm from the 13.3-μm channel yields similar results to the 6.5–10.7-μm technique for mature cumulus clouds, but is much different for immature cumulus. The 13.3-μm channel detects radiation from the middle and lower troposphere. As a result, for opaque cumulonimbus cloud tops, the 13.3–10.7-μm difference yields values near zero because the 13.3- and 10.7-μm bands detect equivalent T_B's. The 13.3-μm channel is more sensitive to thin cirrus (i.e., colder T_B than the 10.7-μm channel), and is a better indicator of low cloud development (deepening) as compared to the 6.5/6.7–10.7-μm technique. Cumulus clouds in a pre-CI state exhibit difference values ranging from −25 to −5 K with the events of the independent dataset.

c. Cloud-top temperature trends

RR03 found that monitoring the drop in satellite-detected 10.7-μm T_B from 0° to −20°C, in addition to cooling rates of −8°C over 15 min (their "vigorous growth" criteria), are important precursors to storm initiation for the cases examined in their study. A cooling rate of −4°C per 15 min corresponds to "weak growth" of cumulus clouds. It was assumed by RR03 that once clouds grow to a height where cloud tops radiate at subfreezing T_B's, the ice nucleation process initiates and the development of precipitation occurs in cold-type continental clouds. An important relationship was observed between satellite and radar data during this critical period. Following the drop to 0°C on satellite, approximately 15 min elapsed before a precipitation echo (>5 dBZ) was detected on radar. As clouds continued to cool, an additional 15 min elapsed before echoes greater than ~35 dBZ were observed. Reflectivities greater than 35 dBZ are typical thresholds used to track the movement of thunderstorms (Mueller et al. 2003; RR03). Therefore RR03 conclude that, by monitoring via satellite both cloud-top cooling rates and the occurrence of subfreezing 10.7-μm T_B's, the potential for up to 30-min advance notice of CI, over the use of radar alone, is possible.

The algorithm presented in this study extends the work of RR03 by incorporating the ability to track moving cloud features. To account for cloud motion in the time interval between satellite images, this study incorporates the VIS and IR satellite-derived AMV identification algorithm of Velden et al. (1997, 1998) toward the formation of satellite-derived offset vectors (SOVs) for evaluating cloud-top T_B and multispectral-band-difference trends. A SOV is defined as the number of 1-km pixels in the latitudinal and longitudinal direction that a given cumulus cloud pixel has moved in the time interval between two satellite images. The SOV is calculated by 1) decomposing the speed and direction provided by the AMV algorithm into u and v components, 2) multiplying the u and v motion components by the time interval between images, and 3) dividing this quantity by the pixel resolution to obtain the number of pixels in the u and v directions that a cumulus cloud pixel has moved between images. The procedure for obtaining mesoscale AMVs (and thus SOVs) is described more completely in Bedka and Mecikalski (2005).

Four interest fields result from the analysis of 10.7-μm cloud-top cooling rates for moving cumulus using SOVs, in correspondence with the results of RR03: 1) cloud-top cooling rates greater than 4°C (15 min)$^{-1}$, 2) cloud tops that have exhibited sustained cooling for a 30-min period [i.e., ΔT_B (30 min)$^{-1}$ > ΔT_B (15 min)$^{-1}$], and 3) subfreezing cloud-top T_B's alone, and 4) cloud-top T_B's that have dropped from above to below freezing within the t to $t − 30$ min time interval. The weaker of the two RR03 cooling rates (4° versus 8°C) was selected in order to provide a conservative identification of clouds that may be slowly evolving into cumulonimbus.

In addition to being able to use 15- and 30-min cloud-top cooling rates to monitor for CI, time differencing of the 6.5 (or 6.7)–10.7-, 12.0–10.7-, and 13.3–10.7-μm multispectral techniques [i.e., $\partial(6.5/6.7–10.7\ \mu m)/\partial t$ and $\partial(6.5/6.7–13.3\ \mu m)/\partial t$] for moving convection can be performed by applying SOVs. As both of these channel differences are typically negative, except in the presence of deep, cold clouds, time trends of these quantities will be positive for growing cumulus. This holds true because smaller negative values in current imagery minus greater negative values in past imagery result in positive time differences. The interpretation of both of these multispectral channel differences is to some extent analogous to that of 10.7-μm temporal differencing. The larger the values of $\partial(6.5/6.7–10.7\ \mu m)/\partial t$, the more rapidly the cloud is deepening; should this time trend become negative, it indicates diminished deepening or a decreasing cloud-top height (Schmetz et al. 1997). For temporal trends of 6.5/6.7–10.7 μm and 6.5/6.7–13.3 μm, values ≥3°C over 15 min are observed to precede CI in the dependent dataset; 12.0–10.7-μm time trends of >2°C were observed to precede CI.

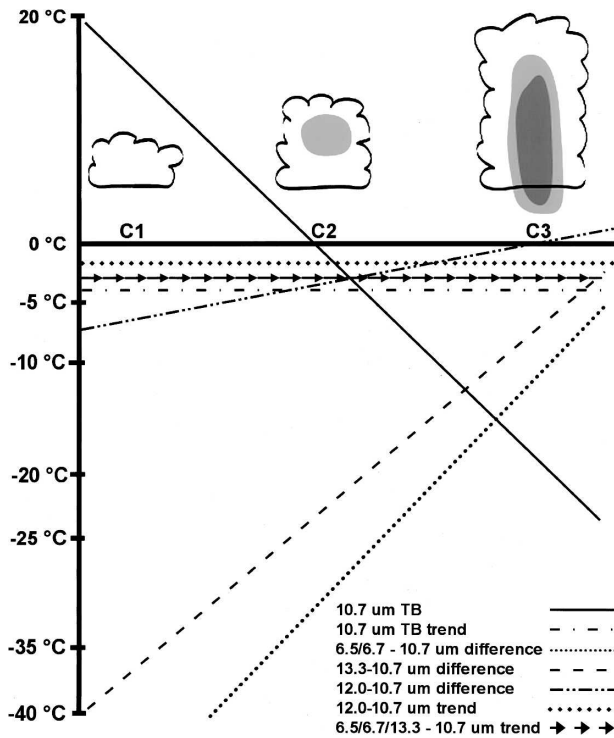Figure 2 schematically presents the behavior of each

FIG. 2. Schematic that demonstrates the relationship between IR channel values, channel differences, and difference trends as a cumulus cloud grows in depth. Cloud "C1" depicts a cumulus in the early stages of growth with no radar echo, "C2" is a cumulus producing an initial echo ≥10 dBZ (mostly elevated), while "C3" shows a cloud with significant vertical development possessing an echo >35 dBZ falling toward the ground. The line plot depicts via seven lines the eight CI interest fields used in the assessment of CI: 10.7-μm T_B values and trends, and 6.5–10.7-, 12.0–10.7-, and 13.3–10.7-μm T_B differences and difference trends. Lightest gray shading is ≥10 dBZ, with darker shading >35 dBZ echo. In this figure, Δt is taken to be 15 min. Scales on left side of graph relate to the critical values of each CI interest field as shown in Table 2. See text for further details.

interest field for an idealized case of CI, in particular, the relationships between IR channel values, channel differences, and difference trends as a cumulus cloud grows in depth (clouds "C1" to "C3"). Figure 2 then graphically illustrates the above relationships and should be compared to Table 2.

d. CI nowcasts

To provide nowcasts of CI using IR satellite indicators, a scoring system that sums the positive indicators is applied. A summary of the criteria incorporated into this scoring system is presented in Table 2, which justifies the use of eight predictor fields from GOES; in essence, redundant information exists across several of the IR interest fields (see Table 1). For the nowcasting assessments, one point (score) is assigned to each pixel

when an interest field criterion is met. Satellite pixels that meet at least seven of eight criteria have been determined to represent rapidly growing, immature (nonprecipitating) cumulus in a pre-CI state. *The underlying premise in this methodology is that immature cumulus exhibiting recent signs of development will continue to evolve into precipitating convective storms, provided that the cloud has access to a sufficient atmospheric boundary layer (ABL) or elevated moisture-convergence source.*

3. Results

The application of the techniques described above will focus on three diverse events, in terms of convective storm regime and atmospheric character. The chosen events are 1) severe and nonsevere convection occurring on 12 June 2002 over the IHOP_2002 domain, 2) tornadic supercell thunderstorms on 4 May 2003 over Kansas, and 3) weakly organized summertime convection on 3 August 2003 over the upper Midwest. These demonstrations focus on locations of robust convective development and culminate in the demonstration of CI nowcasts.

The IHOP case exemplifies the use of 5-min (versus 15 min) *GOES-11* satellite imagery in our AMV processing. The 4 May 2003 event represents a relatively uncomplicated event in terms of cloud-motion fields and CI, as storms initiated along a frontal boundary in eastern Kansas in a relatively uniform motion field; both cases I and III possess more complicated and challenging motion fields for tracking growing cumulus in *GOES-12* data. For case I especially, each of the eight interest fields in Table 2 are described in the satellite imagery as they relate to CI.

a. Case I: 12 June 2002 (IHOP_2002)

For this event (Figs. 3–9), convection developed along a strong ABL moisture gradient across the Texas pandhandle and Oklahoma during the afternoon of 12 June 2002. A mesoscale surface low pressure system over the Texas panhandle produced a zone where dry air converged with a very moist air mass from the Gulf of Mexico along a dry line, which helped trigger strong/ severe thunderstorm development. Convective initiation for this particular case has been relatively well studied by scientists participating in the IHOP_2002 experiment and is the focus of other publications within this special issue (see Markowski et al. 2006). We will focus our analysis on the time period from 2030 to 2130 UTC as CI occurred across Texas and Oklahoma.

Satellite data valid at: 2034 UTC 12 June   2002

Visible Brightness
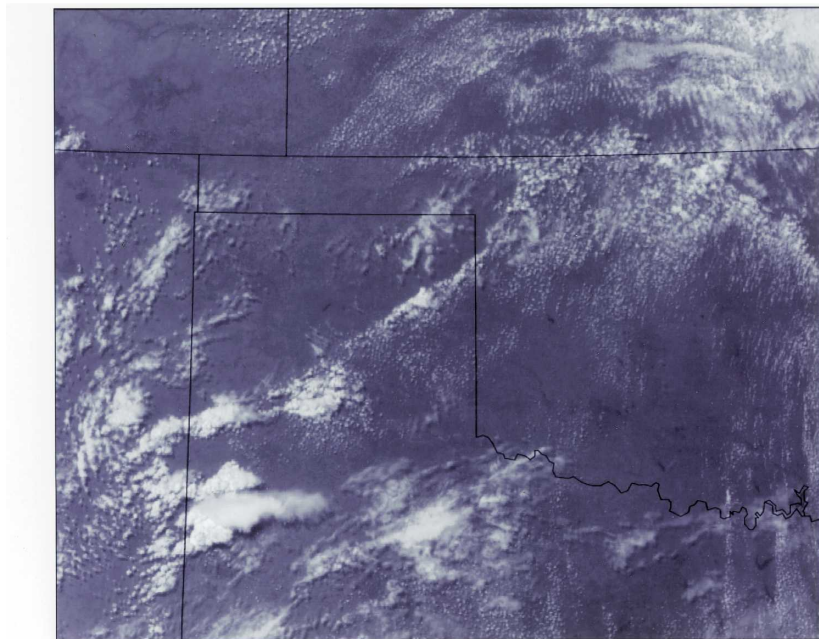
Satellite data valid at: 2034 UTC 12 June   2002

Cumulus Mask: Immature Cu (Red), Mature Cu and Cirrus Cloud (Green)
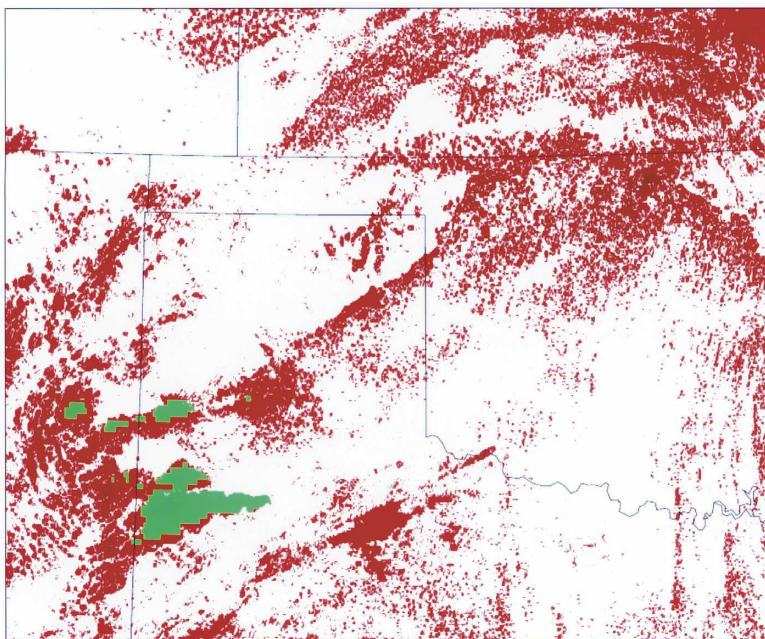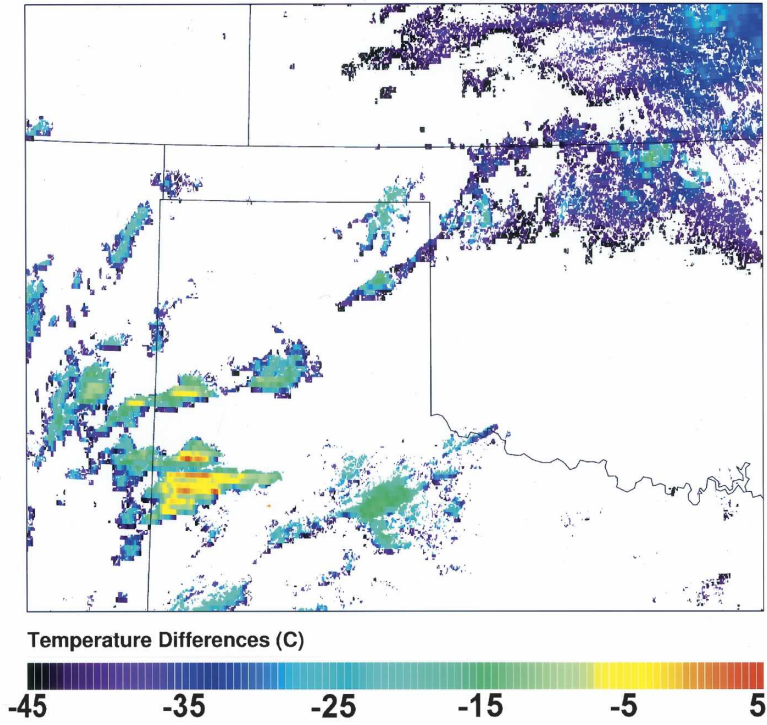

FIG. 3. (a) The 1-km-resolution *GOES-11* visible image for 2034 UTC 12 Jun 2002. (b) The convective cloud mask at same time. In (b), red pixels indicate "immature" nonprecipitating cumulus clouds, while green pixels denote cirrus anvils and cumulonimbus. See text for description.

Satellite data valid at: 2034 UTC 12 June   2002

6.7 - 10.7 μm

Temperature Differences (C)

-45   -35   -25   -15   -5   5

Satellite data valid at: 2034 UTC 12 June   2002

12.0 - 10.7 μm

Temperature Differences (C)

-10   -7.5   -5   -2.5   0   2.5
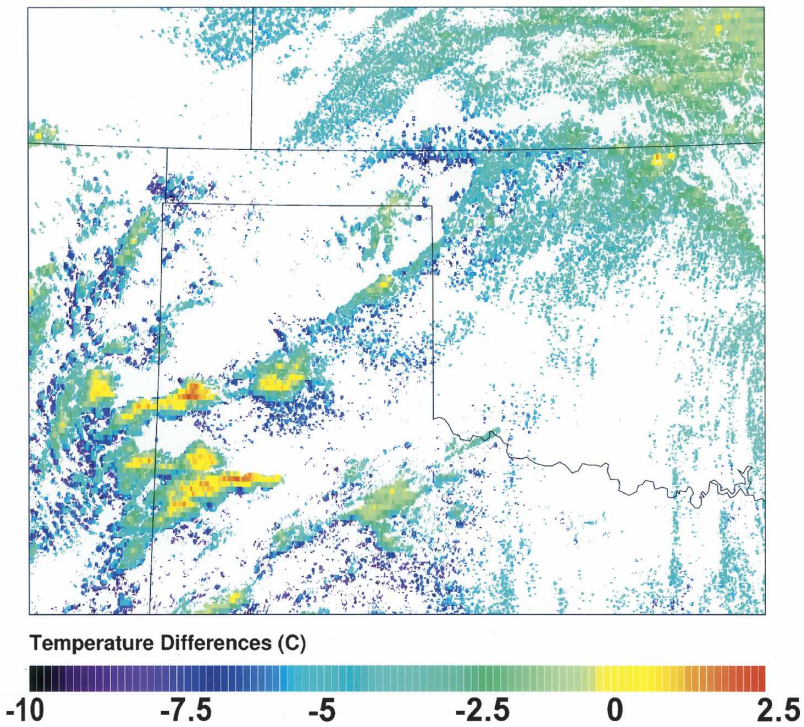
FIG. 4. Multispectral-band-differencing techniques at 2034 UTC on 12 Jun: (a) the
6.7–10.7- and (b) the 12.0–10.7-μm difference.

Satellite data valid at: 2034 UTC 12 June   2002

Satellite-Derived Wind Analysis
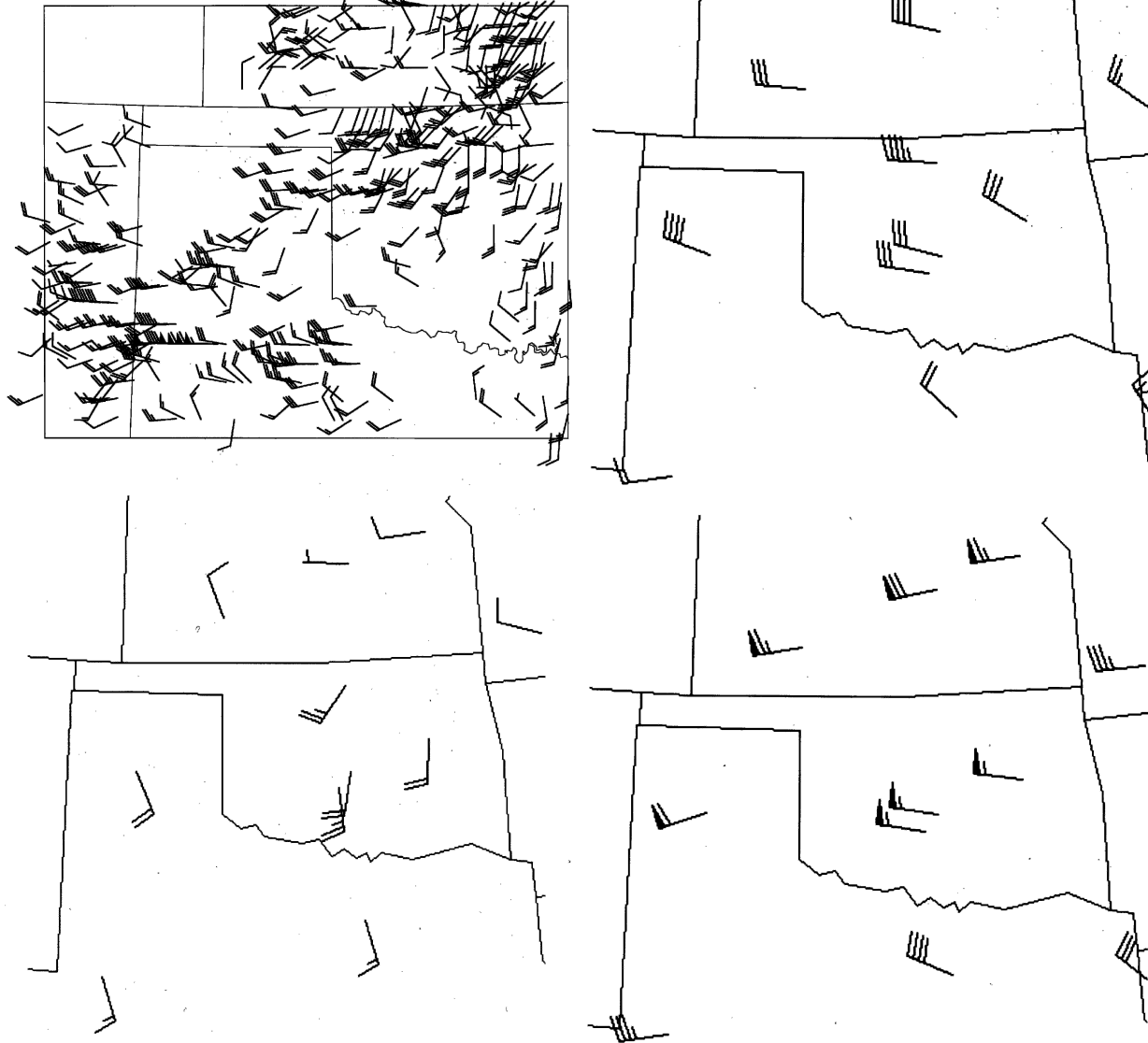
FIG. 5. (a) The VIS and IR satellite AMV analysis (in kt) at 2034 UTC on 12 Jun 2002 (only 1/15th of the AMV field is shown for clarity), (b) 85-kPa radiosonde wind observations at 0000 UTC on 13 Jun, (c) 50-kPa wind observations, and (d) 25-kPa wind observations. Barnes (1964) objective analysis was used to grid the AMVs in Fig. 5a.

A comparison of the convective cloud mask to *GOES-11* visible imagery at 2034 UTC is provided in Figs. 3a and 3b. When compared to the GOES 1-km VIS image, this technique performs quite well in identifying only convective clouds and assessing their relative state (immature versus mature); the CI interest fields will be calculated only where convective clouds are found.

The 6.7–10.7- and 12.0–10.7-μm band-difference techniques at 2034 UTC are shown in Figs. 4a and 4b, respectively. Absolute differences greater than $-10°$ (for 6.7–10.7 μm) and 0°C (for 12.0–10.7 μm) are found to correspond well with cumulonimbus (i.e., mature cu-

mulus) and cirrus clouds in the convective cloud mask. As previously stated, clouds with tops near the tropopause do not need to be monitored for future CI. Clouds with channel differences shown in Table 2 correspond to immature cumuli that have either not begun to precipitate or have reflectivities below the 35-dBZ CI threshold (as determined through comparison of many satellite pixel values against collocated WSR-88D imagery within the dependent dataset).

The VIS and IR AMV analysis, used to evaluate cloud-top T_B and multispectral-band-differencing trends, is shown in Fig. 5a. Only a small fraction (~7%)

Satellite data valid at: 2034 UTC 12 June   2002

Temporal Differencing of 10.7 μm Band (Using Satellite Winds)

Temperature Differences (C)

-50   -40   -30   -20   -10   0

Satellite data valid at: 2034 UTC 12 June   2002

Temporal Differencing of 10.7 μm Band (Using Satellite Winds)

Temperature Differences (C)

-50   -40   -30   -20   -10   0

Satellite data valid at: 2034 UTC 12 June   2002

Temporal Differencing of 6.7-10.7 μm Difference

Temperature Differences (C)

0   10   20   30   40   50
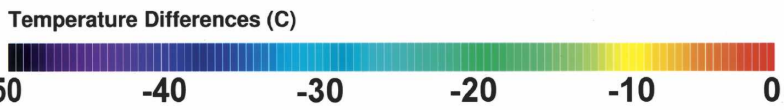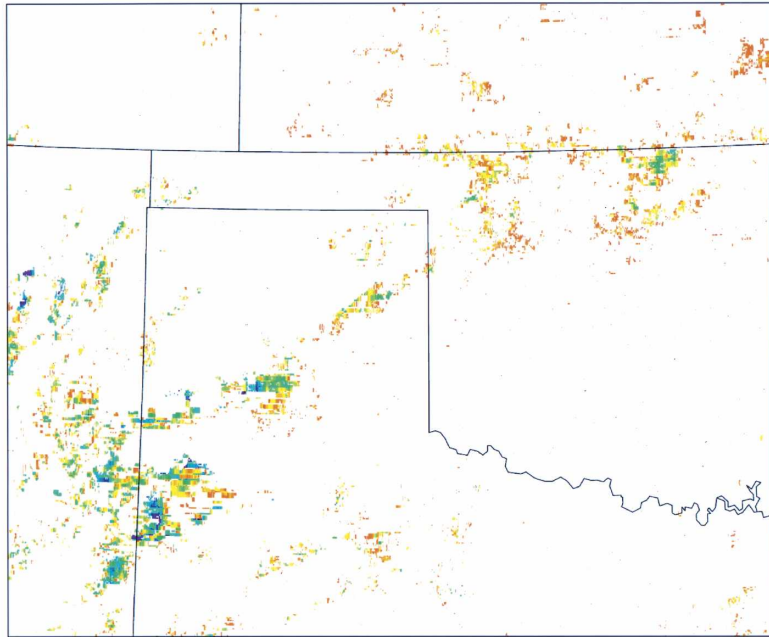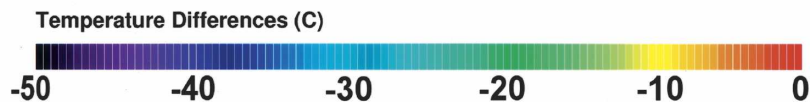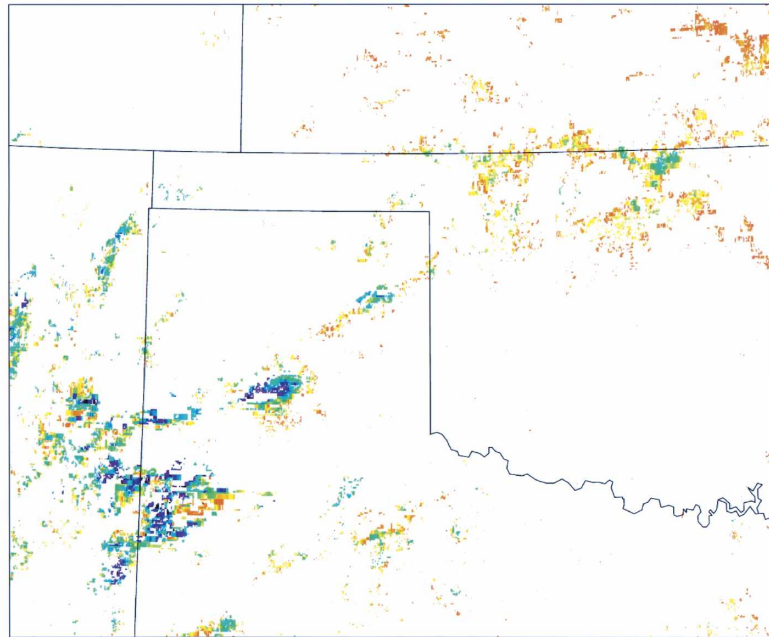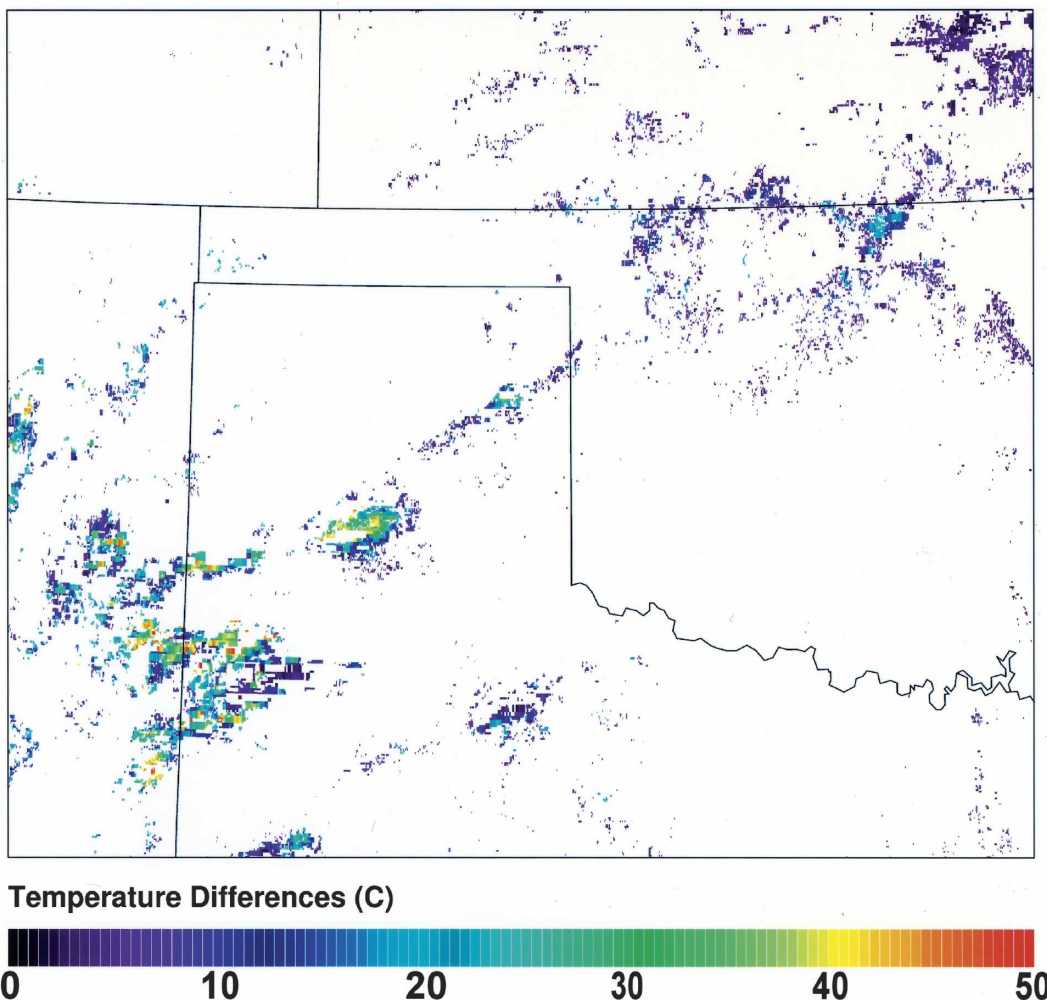
FIG. 7. Thirty-one-minute trend of the 6.7–10.7-μm channel difference, ending at 2034 UTC 12 Jun 2002. Larger positive values indicate rapidly growing cumulus, whereas smaller values suggest cumulus undergoing slow or no growth. Negative values (none shown) indicate dissipating cumulus.

of the barbs are shown so that one can better visualize the overall cloud-motion field. The AMV analysis illustrates a complicated low-level flow over southwest Kansas, as well as distinct flows associated with each of the two cloud categories identified by the convective cloud mask (green versus red in Fig. 3b) applicable to the cloud types within the image. Immature cumuli are seen to move generally from the southwest to northeast at speeds of 20–40 kt. The exceptions to this general flow include a cyclonic circulation over southwest Kansas, and westerly flow in north Texas. Also, the motions of the mature, taller cumulus and their associated cirrus anvils are greater westerly-southwesterly at speeds >50 kt. This variation in cloud motion with height can also be seen in the radiosonde observations presented as Figs. 5b–d, which encourages the use of these AMVs to derive SOVs for cloud-top trend assessments.

The proper use of SOVs is very dependent upon the

$\leftarrow$

FIG. 6. *GOES-12* 10.7-μm cloud-top T_B time trends for (a) 14- and (b) 31-min intervals at 2034 UTC. Time trends are greatest for cumulus in eastern New Mexico, and along a line from the central Texas panhandle to north-central Oklahoma.

Satellite data valid at: 2034 UTC 12 June   2002
Nowcast for Future CI (red), Cirrus and Mature Cu (grey)
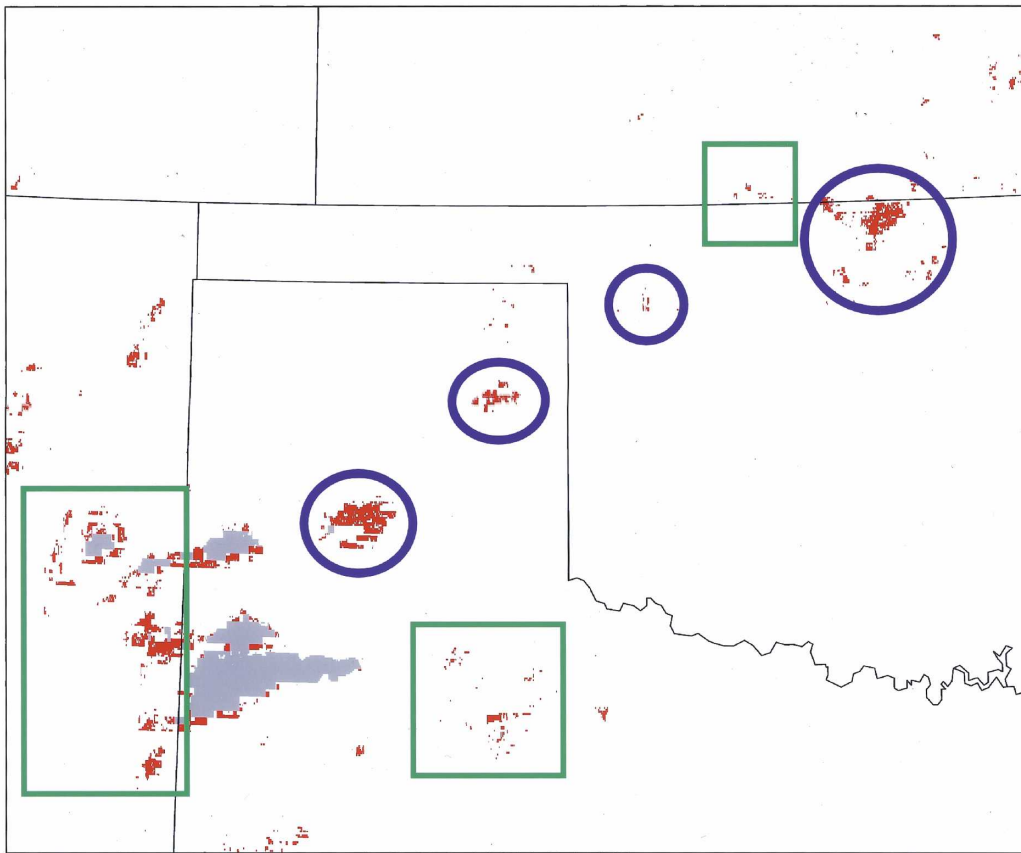

FIG. 8. The CI nowcast product valid at 2034 UTC on 12 Jun 2002. Pixels highlighted in red have met at least seven of the eight CI criteria and need to be monitored for future CI over the following 30–45 min. Gray pixels represent mature cumulus and cirrus from the convective cloud mask. Circled regions are considered "successful" CI forecasts. The red pixels in the squared region over New Mexico, although possessing thunderstorms, seem to be less associated with new CI (rather continued development of existing storms with >35 dBZ echoes). The square regions in extreme south-central Kansas are an example of our method's failure, yet one that may be influenced by proximity to the Vance Air Force Base radar site and associated ground clutter echoes. See text for description.

accuracy of the AMV processing algorithm, with errors in satellite-derived motion resulting in the incorrect determination of past pixel locations and cloud-top trends. In particular, a significant contribution to cumulus tracking problems using SOVs is that cumulus clouds undergo significant changes on scales of tens of minutes. Simply choosing to monitor larger cumulus (scales of 3–8 km in width) eliminates some of the problems associated with cloud dissipation and cloud replacement caused by subsampling (i.e., one cumulus dissipates, only to be replaced by another in about the same location 15–45 min later), which we have not implemented here. Use of 5-min time resolution GOES imagery (or higher), as used in this case, provides optimal SOV estimates.

The 14- and 31-min 10.7-μm cloud-top cooling trends

are shown in Figs. 6a and 6b. We have chosen to show the 14- and 31-min fields as the 5- and 10-min time cloud-top T_B trends of these fields are often too small for discussion purposes. In addition, the 10.7-μm CI interest field criteria from RR03 were developed from the use of 15-min data, not the 5-min resolution data available with *GOES-11*. The 10.7-μm cloud-top T_B images at 2003, 2020, and 2034 UTC are not shown. Noteworthy in these figures, clouds undergoing CI (in far eastern New Mexico, and along a line from Amarillo, Texas, to north-central Oklahoma) possess the more significant cooling trends in the image, generally from $-20°$ to $-40°$ over 14- and 31-min periods. A comparison of the 31-min trend in the 6.7–10.7-μm technique (Fig. 7) to 31-min trends in 10.7-μm T_B (Fig. 6b) illustrates the correspondence between positive values of
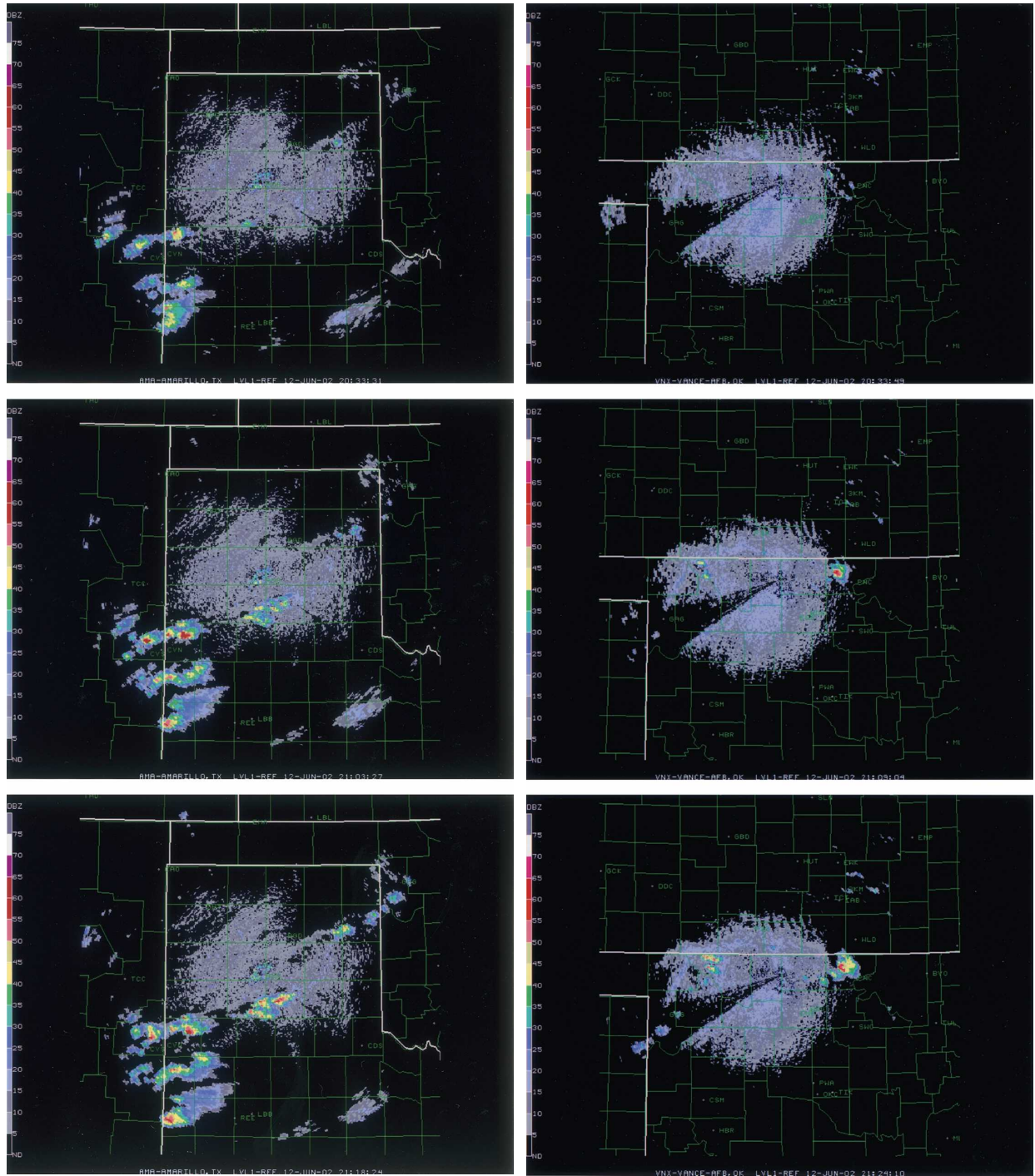
FIG. 9. Next-Generation Weather Radar (NEXRAD) WSR-88D composite reflectivity mosaics at (a) 2033, (b) 2103, and (c) 2118 UTC for Amarillo, TX, and (d) 2033, (e) 2109, and (f) 2124 UTC for Vance Air Force Base, OK. All data valid on 12 Jun 2002, illustrating the evolution of the convective storm event [courtesy of National Center for Atmospheric Research, Research Applications Program (NCAR-RAP)]. Data also used to validate CI nowcasts in Fig. 8.

the multispectral differences and cloud-top cooling rate. Positive time trends in 6.7–10.7-μm channel differences imply that a cloud top is growing into increasingly dry air in middle or especially upper-tropospheric levels and/or is nearing the local equilibrium level or tropopause. For the $\partial(12.0-10.7)/\partial t$ μm differences (not shown), positive trend values also indicate a growing cloud and a cloud top above the 0°C isotherm.

A map of future CI can be produced by combining the eight CI interest fields for all 1-km pixels. Pixels that meet at least seven of the eight criteria as outlined in Table 2 have been highlighted in red in Fig. 8 (at 2039 UTC) for case I and provide a forecast of CI over the following 30–45 min. A red pixel therefore represents a vertically developing, newly glaciated cumulus with a cloud-top T_B within the 0° to −20°C range (from RR03) that meets seven CI criteria. Pixels highlighted in gray represent mature cumulus that are likely already precipitating (cumulonimbus) or cirrus clouds, and have been omitted from processing. A comparison of the red pixels in Fig. 8 to future radar imagery, at 2103 and 2118 UTC [Figs. 9b,c for Amarillo] and at 2109 and 2124 UTC [Figs. 9e,f for Vance Air Force Base, Oklahoma], demonstrates the algorithm's accuracy; this is also seen when comparing Figs. 3a and 8. This nowcast captured the future development of convection across the Texas panhandle and into Oklahoma (outlined by ovals). Convective cells in the central Texas panhandle and north-central Oklahoma were producing <15 dBZ echoes at 2033 UTC (Figs. 9a,d), which increased to ~45 dBZ by 2103–2109 UTC (Figs. 9b,e) and >55 dBZ by 2118–2124 UTC (Figs. 9c,f). Other CI nowcast pixels in the northeast Texas panhandle also reached the 35-dBZ threshold by 2118 UTC (Fig. 9c), indicating again nowcast skills for ~30 min lead times (circled regions).

A moderate degree of noise and "false alarms" are present in the CI nowcast for this case. Some CI nowcast pixels in the south-central portion of the domain appear to correspond with ~15 dBZ echoes at the time of the nowcast that never evolved beyond the 35-dBZ CI threshold (e.g., boxed region in extreme south-central Kansas, near the Vance radar site). Other nowcast pixels in this region were simply inaccurate. Difficulty exists in assessing the nowcast skill for pixels in the southwest portion of the domain near the Texas–New Mexico border (outlined by boxes). An examination of the radar imagery reveals that an enhancement of convection did occur for cells along the Texas–New Mexico border 30–45 min after the CI nowcast was made. Much of this enhancement occurs in New Mexico where the CI nowcast pixels were present, and an examination of satellite imagery revealed that cumulus in this region continued to grow vertically over time. Reflectivity associated with much of the New Mexico convection appears to be near or slightly below the 35-dBZ threshold, however at the 2030 UTC CI nowcast time. These cumuli were located within a relatively dry ABL air mass and were induced by solar heating along the high terrain of eastern New Mexico. The lack of sufficient ABL moisture likely inhibited efficient precipitation production for cumulus in this region. Problems associated with satellite-based CI nowcasting in regions of limited ABL moisture will be discussed in section 4. Most of the other false alarms can likely be explained by the following: 1) small SOV errors can produce 10.7-μm cooling trends of greater than 4°C (15 min)$^{-1}$, 2) the 6.7- and 12.0-μm channels for *GOES-11* have a resolution of 8 km, which leads to inaccuracies associated interpolating the 6.7–10.7-μm difference and time trend to the 1-km VIS resolution.

Despite the problems associated with this case, the CI nowcast demonstrates a high degree of skill in capturing the primary convective development across the Texas panhandle and Oklahoma. From this, we propose that optimal CI nowcasts are produced when satellite imagery has both high temporal (≤5 min for SOV estimation) and spatial resolutions (≤4 km). *The premise of the assessment in Fig. 8 is that linear trends in cumulus development will continue in the future.* Under this assumption, *the algorithm identifies locations where the mesoscale convergent forcing is supporting organized updrafts of sufficient scale to produce precipitation and the upscale growth of cumulus clouds.*

The following two cases represent further tests of the above methods. Provided the detailed description for case I, generally only the primary results are presented for the remaining events.

b. Case II: 4 May 2003

For this event, a strong, slow-moving spring storm served as the focal point for a severe thunderstorm outbreak across much of the U.S. southern plains (i.e., the IHOP_2002 domain) on 4 May 2003. At least 90 tornadoes touched down in eight states including 39 in Missouri and 15 in Kansas within this event, along with many reports of hail and high winds. Attention will focus on the time period from 1930 to 2100 UTC as convective storms were rapidly developing throughout the state of Kansas. As shown in Figs. 10a–d, several storms within region 1 (regions outlined in boxes and labeled as "1" and "2" within Fig. 11a) evolved into tornadic supercells, while those in region 2 organized in a linear fashion, with embedded severe cells.

Unlike case I, this event makes use of 15-min-resolution *GOES-12* imagery to calculate SOVs and cloud-top T_B/multispectral technique trends. Slightly less accurate SOVs are obtained as a result, yet high quality 30–45-min CI nowcasts are obtained. As a result of using *GOES-12*, two interest fields are different because of the change to the 13.3-μm versus 12.0-μm channel (see Table 2).

Comparison of immature and mature cumulus cloud motions (Fig. 12a) to synoptic upper-air observations at

85 and 25 kPa (Figs. 12b,c) are presented as a strong indication that both the AMV speed and direction are in close agreement with reality. This case demonstrates this AMV–upper-air wind comparison very well given the less complicated wind field compared to case I. The motion of immature clouds within region 2 differs from those of region 1 as low-level flow shifts to the west-southwest upstream of a lower-tropospheric trough axis passing through western Kansas at this time. This demonstrates that the AMV processing scheme of Bedka and Mecikalski (2005) can accurately estimate the motion of cloud features with varying heights.

The 10.7-μm cloud-top cooling rates $< -4°C$ (see Figs. 13a–c), calculated using the RR03 technique (Figs. 14a,c) and SOV differencing, (Figs. 14b,d) are presented for both 15- and 30-min time intervals. A comparison of the 15-min cooling rates for the two techniques yields differences in both location and magnitude of cooling maxima, especially in the southwest portion of region 2. The RR03 technique (Fig. 14a), which does not account for cloud motion, indicates that many convective clouds in southwest Kansas exhibit cooling rates $>30°C$, much greater than what actually occurred (Fig. 14c). This disparity is caused by the movement of convective cloud features within the 15-min period between these two images. Clear pixels at 1945 UTC that have become cloudy by 2000 UTC are assigned spurious cooling rates, equal the difference between the cloudy and clear T_B's. This is more evident at the 30-min time lag (Fig. 14b compared to Fig. 14d) and for clouds in region 2, which moved appreciably in the 15–30-min time interval. A closer agreement between these two techniques exists within region 1 because the clouds propagate along a south-southwest–north-northeast axis, thereby resulting in only a slight movement for the primary line of convection.

The CI nowcast shown in Fig. 11a identifies future development of the primary convective line in region 1, as well as convection in region 2. Pixels identified in southeast Kansas and western Missouri also evolved into precipitating convective storms (not shown in radar imagery). For this particular case, predictive skills are shown for moving convective storms at 30–45-min lead times. Preliminary analysis suggests that accuracies of ~60%–70% are obtained when pixel-by-pixel comparisons are made between the CI nowcast pixels (red pixels in Fig. 11a) and echoes ≥ 35 dBZ in subsequent imagery (Fig. 10).

c. Case III: 3 August 2003

An upper-tropospheric, cold-core cyclonic circulation, in addition to lake-breeze circulations surrounding Lake Michigan, triggered numerous, primarily nonse-vere thunderstorms during the afternoon of 3 August 2003. This case was chosen to show that the CI nowcast algorithm is able to identify future CI for an atmosphere characterized by generally weak static stability, and mesoscale forcing associated with a nearly closed upper-level (~50 kPa) low. Figure 15 details the evolution of this event from 1645 to 1815 UTC from the WSR-88D site near Chicago, Illinois (KLOT). The radar imagery at 1715 UTC shows that CI had already occurred in northeast Illinois as well as in southeastern Wisconsin and western Lower Michigan. As the event evolved, CI took place along the Lake Michigan shoreline in Indiana and Michigan (Figs. 15a–d), as well as in many locations throughout Wisconsin and Illinois. The convection in Illinois is particularly interesting, as it organized into three subtle linear features across the western, central, and eastern portions of the state, as seen in the VIS satellite imagery (Fig. 16b).

The CI nowcast product (Fig. 16a) indicates that CI would occur along these three lines, as validated by subsequent radar imagery. In addition, the nowcast also captured the continued development of convection along the lake-breeze front in northeast Illinois as well as new CI in northern Indiana and western Lower Michigan. Because of the slow motion of the convection in this case (≤ 20 kt, especially across Wisconsin and along the Lake Michigan lake-breeze front), it is expected that trend assessments that do not rely on cloud-motion correction would have worked relatively well. Nonetheless, because of the widely variable cloud motions, this case is particularly challenging for the development of reasonable SOVs, which were done accurately based on the validation of CI nowcasts with subsequent radar imagery.

4. Method uncertainty and errors

The method will now be summarized in terms of the uncertainty of the results and likely sources of error. As this technique for nowcasting CI is tested by comparing satellite IR values and trends against WSR-88D radar reflectivity, several issues need to be discussed regarding these analyses. These include 1) monitoring satellite trends while comparing to radar echoes, versus the implied tracking of radar echoes with satellite data, 2) tracking storms using SOVs across a regional area (i.e., SOV errors), 3) the choice of the range of values used when defining each interest field, and 4) the relative importance of each interest field to nowcasting CI (i.e., redundancy of information). The fourth (a subject of ongoing research) involves the uncertainty regarding use of *less than* seven interest fields to positively identify CI at 1-km resolution. Another limitation of this
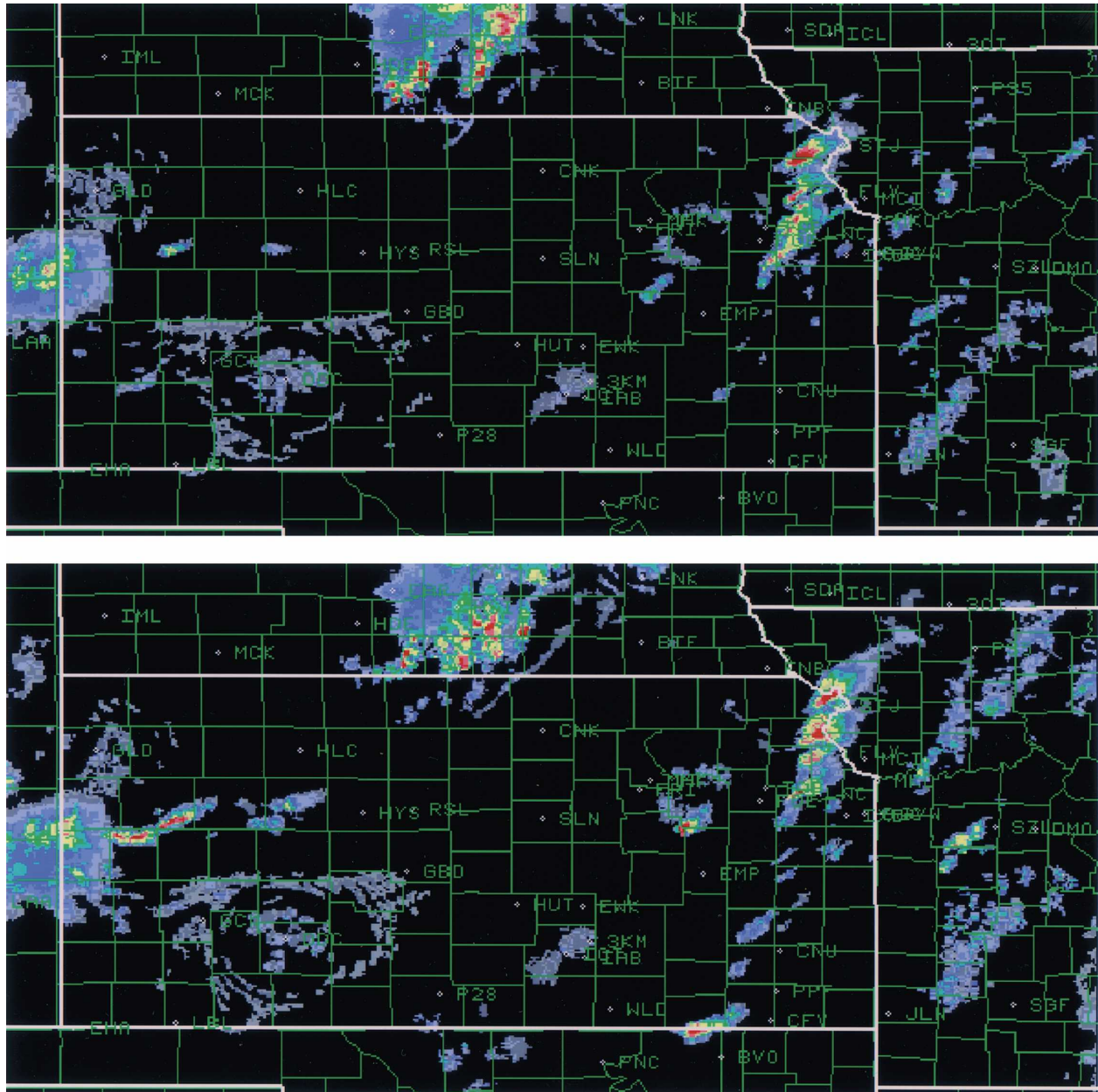
Fig. 10. NEXRAD WSR-88D composite reflectivity mosaics at (a) 1930, (b) 2000, (c) 2030, and (d) 2100 UTC on 4 May 2003 illustrating the evolution of the convective storm event (courtesy of NCAR-RAP).

nowcasting methodology is that the algorithm will behave differently as environments become more tropical (e.g., oceanic convection, island-induced convection), polar, or mountainous (e.g., convection occurring over elevated terrain, convection in cold tropospheric environments). Some level of condition-specific tuning would be needed in these circumstances.

After a CI nowcast is produced, a visual comparison to future WSR-88D radar data is performed to confirm that rainfall, above the 35-dBZ threshold, is indeed oc-

curring at the locations of the nowcast pixels. Within the algorithm, we therefore have not chosen to track radar observations and subsequently link digital radar reflectivity observations (navigated to the GOES satellite projection) to cumulus IR signatures at the pixel scale. There are several reasons for this. Figure 17 schematically illustrates the often-low correlation between radar echoes and satellite clouds (i.e., the IR signatures of convection) at a specific point. Across the area of a developing convective cloud (without an anvil in Fig.
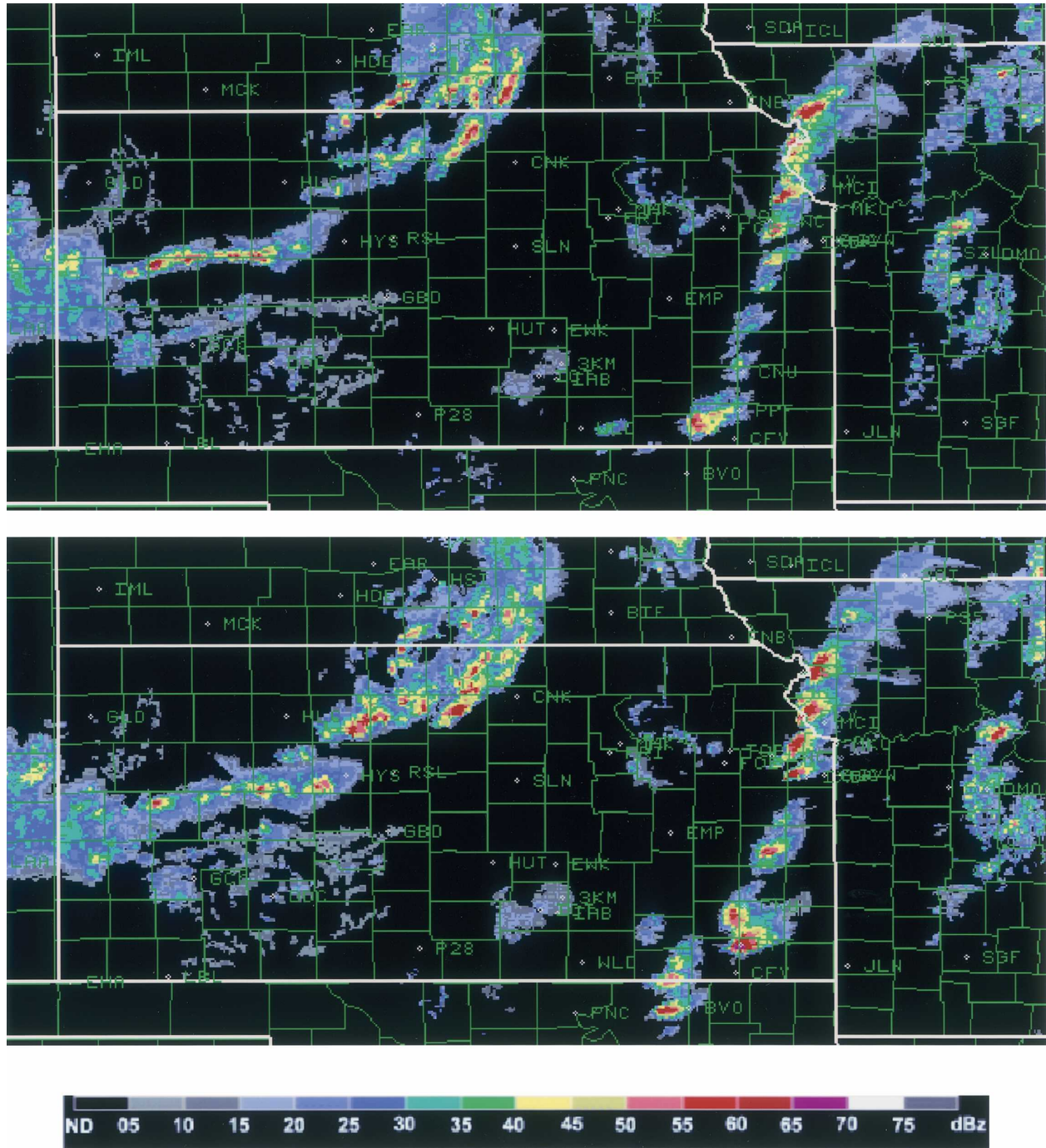
FIG. 10. (*Continued*)

17), which is usually much larger than the area occupied by the precipitation echo, there is no consistent relationship that explains the placement of the echo within the cloud region. Another reason is that radar echoes do not necessarily propagate at the same speed or in the same direction as clouds, especially those measured by satellites (satellite parallax errors being one reason for this). Therefore, tracking radar echoes with satellite observations of convective cloud motion is not reasonable. Outside of operating on small regional scales (e.g., as done in RR03), or incorporating more sophisticated radar and satellite tracking algorithms, performing the analysis as done herein is logical given the satellite datasets relied upon. The situation highlighted in Fig.
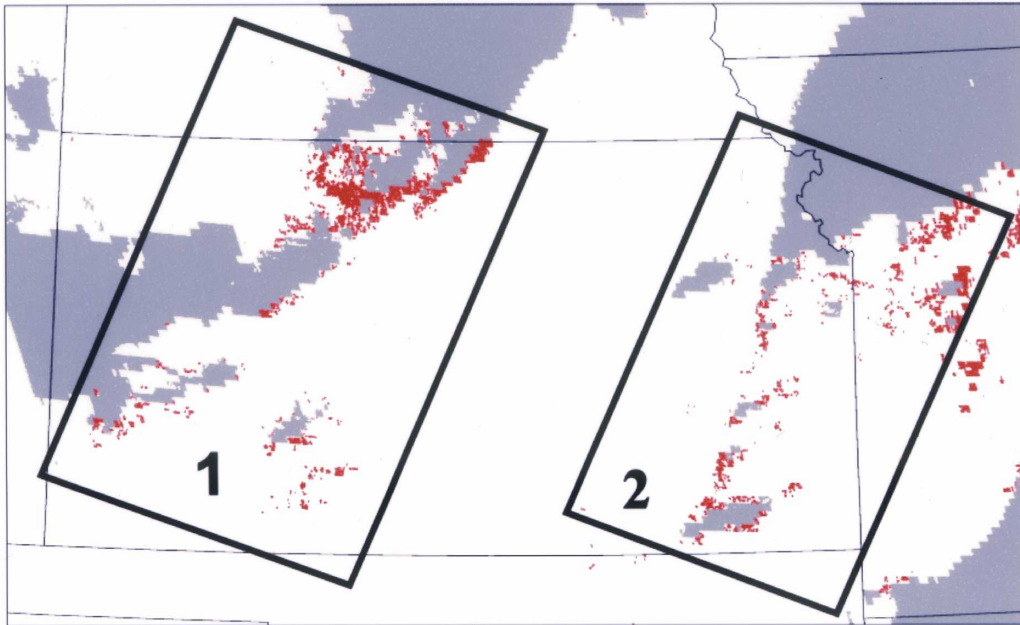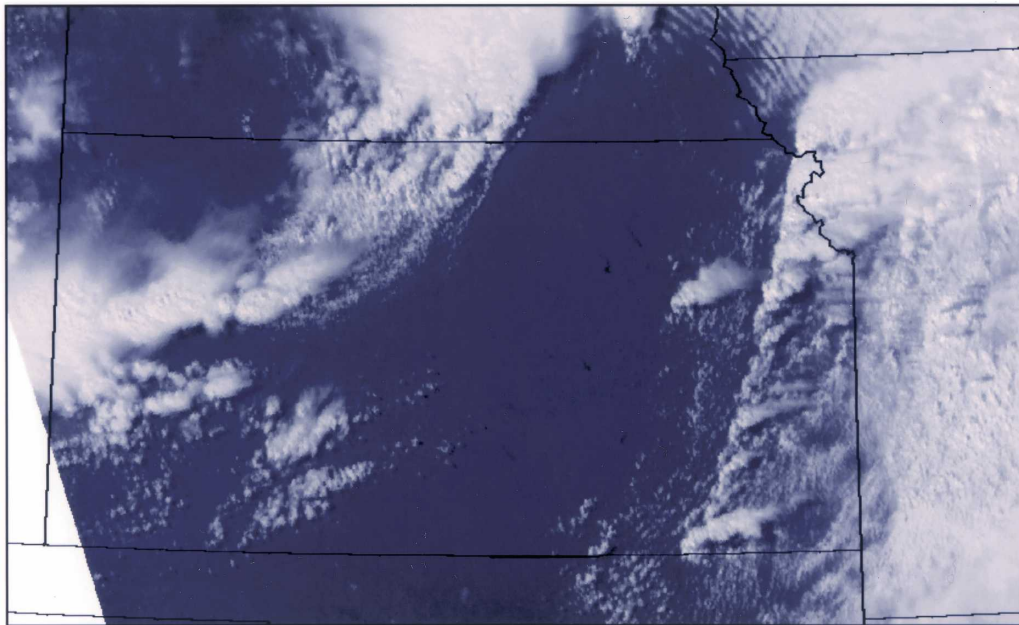
FIG. 11. (a) The CI nowcast product at 2000 UTC on 4 May 2003. Pixels highlighted in red have met at least seven of the eight CI criteria and need to be monitored for future CI over the following 30–45 min. Gray pixels represent mature cumulus and cirrus from the convective cloud mask. (b) A 1-km-resolution *GOES-12* visible image is shown for comparison. Regions labeled "1" and "2" in (a) are the areas of focus for this case (case II).

Satellite data valid at: 2000 UTC   4 May   2003

Satellite-Derived Wind Analysis

FIG. 12. (a) The VIS and IR satellite AMV analysis (in kt) at 2000 UTC on 4 May 2003 (only 1/15th of the AMV field is shown for clarity), (b) 85-kPa radiosonde observations at 0000 UTC on 5 May, and (c) 25-kPa wind observations.

beneath the IR cloud shield for all 1-km pixels; note the stars in each $t = t + 30$ min cloud as examples of positive (top) and negative (bottom) echo-IR field correlations.

As stated, use of SOVs to monitor cumulus cloud motions represents a unique aspect of this research, yet one certainly associated with errors. Over 15 min, simple geometry shows that a SOV in error by ~6.3° in direction with a 10 m s^{-1} motion leads to a ±1 km pixel error in tracking, with a 12.5° SOV direction error causing a ±2 pixel error in tracking, and so forth. With a 20 m s^{-1} motion, a ±1 pixel tracking error occurs with only a 3.2° SOV direction error, with a doubling of this SOV direction error (6.4°) causing a ±2 pixel error. Fortunately then, SOV errors need to be systematically >5° in error before serious degradation results. Being that the IR data are interpolated to the 1-km VIS satellite projection, where a minimum of 16 VIS pixels exist for every one IR pixel, the correct IR trend may still be calculated with an SOV error of ~2 pixels. Although great care is taken to determine the correct SOV by comparing them to cloud motions on the pixel scale, this represents one potential systematic source of error. The cause of poor SOV calculation is generally associated with using nonoptimal VIS or IR AMVs. This tends to be a problem especially when cumulonimbus and cumulus exist in close proximity in highly sheared environments, each possessing different motions (e.g., southerly ABL flow with strong westerly flow aloft). In-line quality control checks, verifying that the processing is indeed tracking a cumulus cloud, mitigates some of this error. In effect then, this algorithm is inherently designed to isolate larger, persistent cumulus clouds (scales ≥5 km). These clouds are in fact most interesting from a CI perspective as they likely possess larger updraft widths "connected" to more persistent and organized surface convergent forcing.

An aspect of this research is determining the relative importance of each interest field to nowcasting CI. As discussed above, this study grows directly from several others, in particular, RR03, Ackerman (1996), Schmetz et al. (1997), and Nair et al. (1999; for cloud identification), and therefore is applying proven research. There are several interest fields used within this study that have not been utilized for convective storm studies (e.g., the 13.3–10.7-μm difference field and its time trend). Ongoing work is attempting to directly match all IR satellite indicators against radar echoes within many convective clouds over limited areas, with preliminary linear-discriminant analysis (using data from this study; not shown) suggesting that ∂ (10.7 μm)/∂t, the 10.7-μm T_B itself, and ∂ (13.3–10.7)/∂t μm are the most important interest fields.

17 exemplifies why statistical error analysis procedures could not be easily and accurately employed in this study. Even though all interest fields may suggest CI, there is no necessity that a ≥35 dBZ echo exist directly
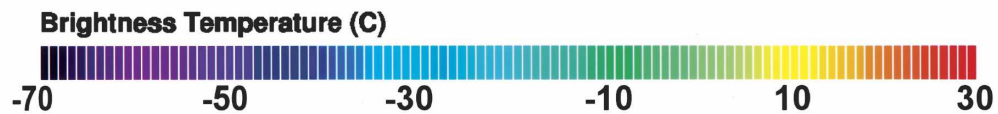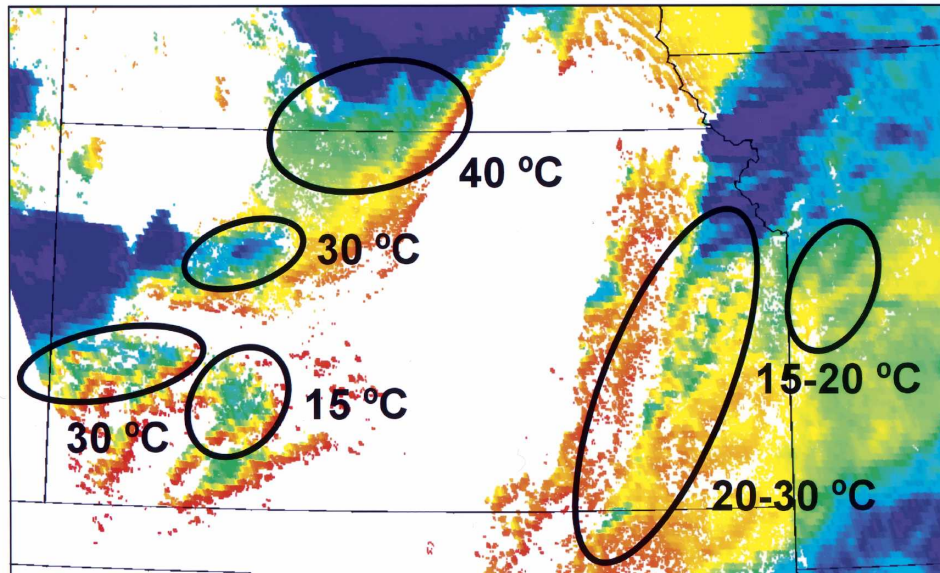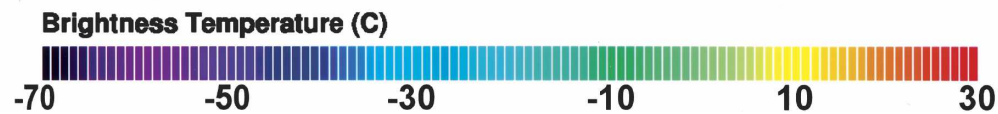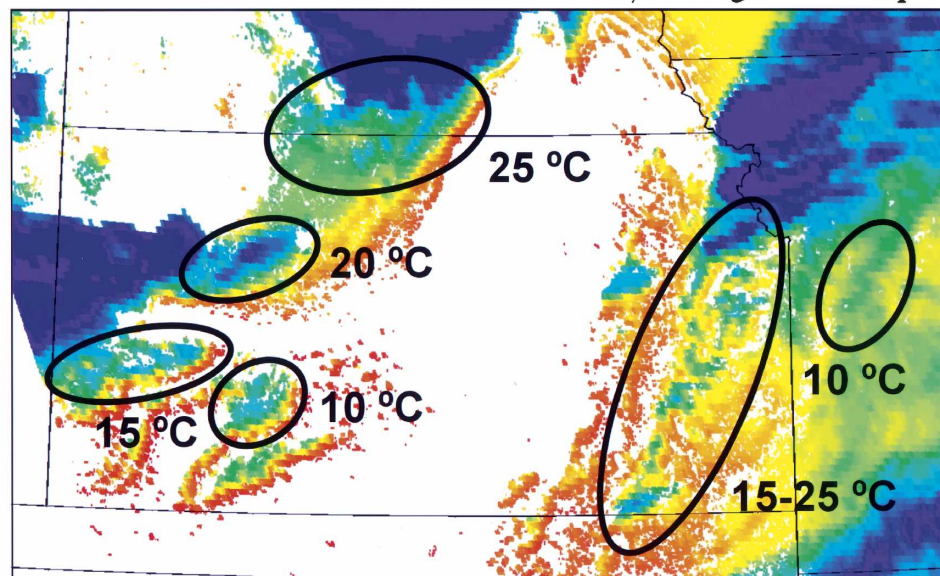
FIG. 13. *GOES-12* color-enhanced 10.7-μm imagery for cumulus clouds at (a) 1930, (b) 1945, and (c) 2000 UTC for the 4 May case (case I). Developing convection is outlined by ovals, and the (a) 30- and (b) 15-min cooling rates (determined by a human expert) are listed for each distinct growing cumulus cluster.
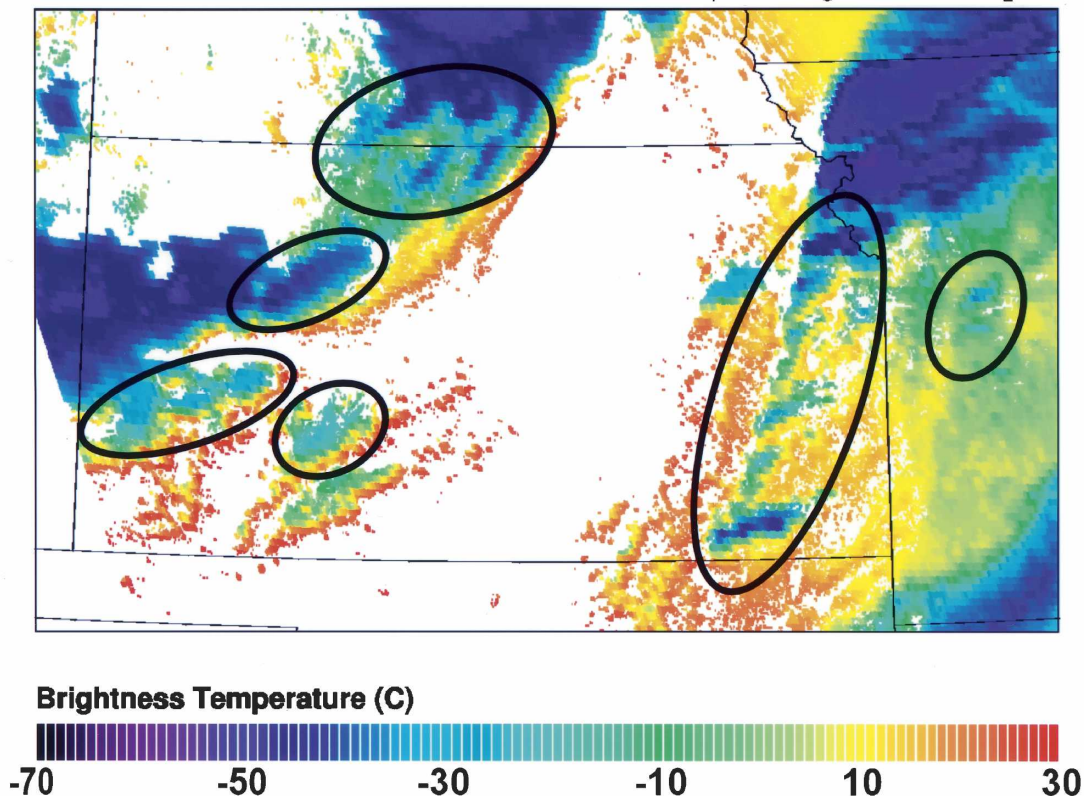
FIG. 13. (*Continued*)

To effectively use the CI nowcast product for real-time operational forecasting, one should couple it to lower-tropospheric moisture and atmospheric stability information to identify if the atmosphere is supportive of convective storm growth. Although seven of eight interest field conditions may be satisfied, a cumulus pixel will not evolve into a cumulonimbus unless it can continually ingest sufficient moisture to initiate ice crystal growth and efficient precipitation production. During the summer, daytime cumulus clouds produced by solar heating of the ABL generally have access to sufficient moisture to allow for upscale growth into a cumulonimbus. During the other three seasons, especially winter, analysis of algorithm output shows that cumulus clouds may meet many criteria while never evolving into cumulonimbus. This often occurs as middle- to upper-tropospheric cold-core vortices propagate over the relatively warm ABL present in the southeastern United States. This synoptic regime often triggers robust cumulus growth beneath the cold vortex, which is identified by the nowcast algorithm. Many times however, these cumuli never engage in upscale growth and ever engage in upscale growth and

precipitation production because of insufficient lower-tropospheric moisture.

5. Conclusions

This study identifies the precursor signals of CI from sequences of 5- and 15-min time resolution 1-km VIS and interpolated IR imagery from GOES. Results indicate that CI may be forecasted up to ~45 min in advance through the monitoring of key IR temperatures/trends for convective clouds. For the IHOP case (case I), over the elevated terrain in New Mexico, results suggest that up to 60-min lead times are possible. Based on these results, *we surmise that the current predictability limitation of this algorithm is ~1 h, as cumulus clouds evolving for longer periods often do not grow to initiate rainfall*. Convective initiation nowcasting is made possible by first interpolating all IR data to the VIS resolution and projection, second by locating only the clouds capable of initiating rainfall within GOES data through using a cumulus cloud mask at 1-km resolution, third by performing several multispectral IR

Satellite data valid at: 2000 UTC   4 May   2003
Temporal Differencing of 10.7 μm Band (No Satellite Winds)

Temperature Differences (C)

-50   -40   -30   -20   -10   0

Satellite data valid at: 2000 UTC   4 May   2003
Temporal Differencing of 10.7 μm Band (Using Satellite Winds)

Temperature Differences (C)

-50   -40   -30   -20   -10   0
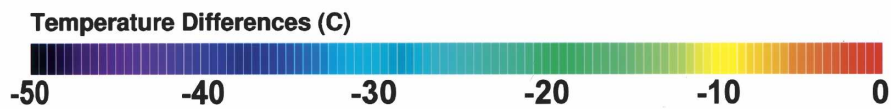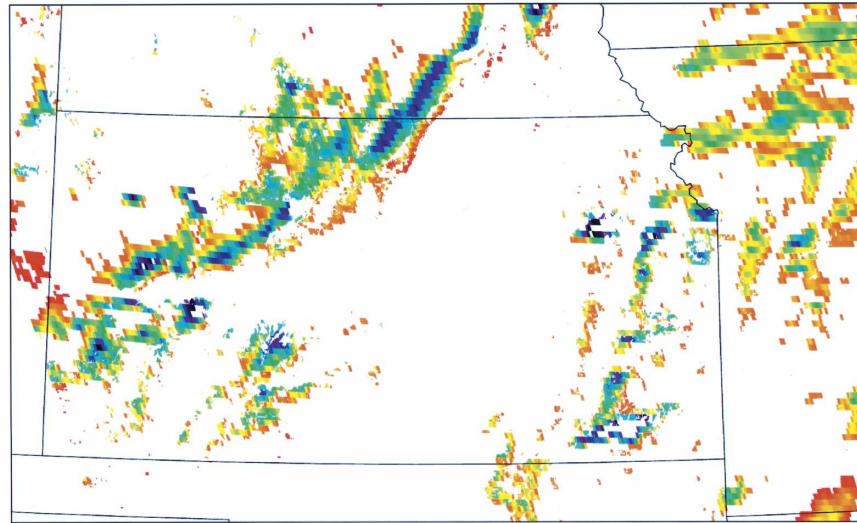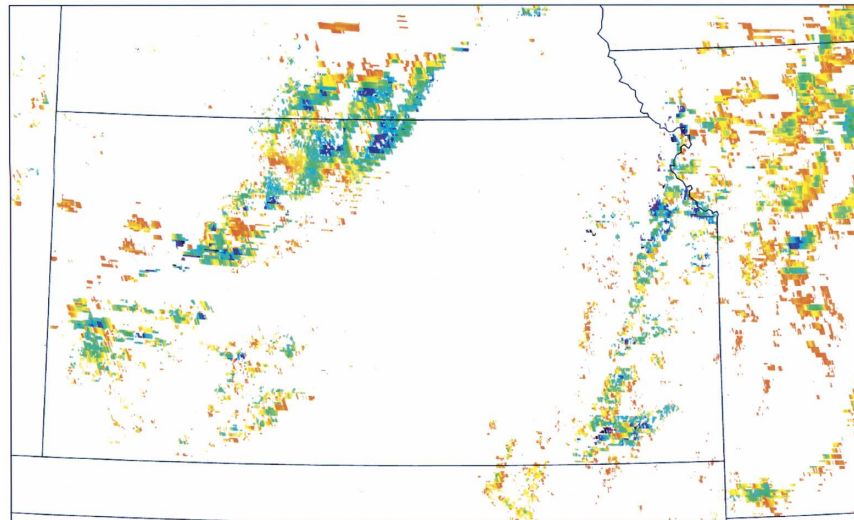
FIG. 14. The 10.7-μm T_B cumulus cloud-top cooling rates, with and without the use of SOVs. (a), (c) The 15- and 30-min cloud-top cooling rates using the RR03 technique (i.e., no cloud motion). (b), (d) The SOVs are employed to track clouds over time. Shown are time differences less than $-4°$C. Note the differences between the two techniques, which can be mainly attributed to storm propagation during the time intervals between images that adversely affects the results of the RR03 differencing method.

Satellite data valid at: 2000 UTC   4 May   2003

Temporal Differencing of 10.7 μm Band (No Satellite Winds)

Temperature Differences (C)

-50   -40   -30   -20   -10   0

Satellite data valid at: 2000 UTC   4 May   2003

Temporal Differencing of 10.7 μm Band (Using Satellite Winds)

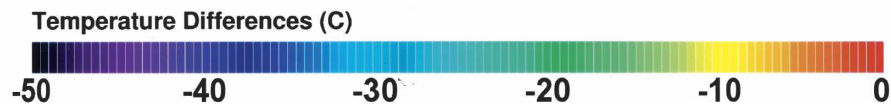**Temperature Differences (C)**

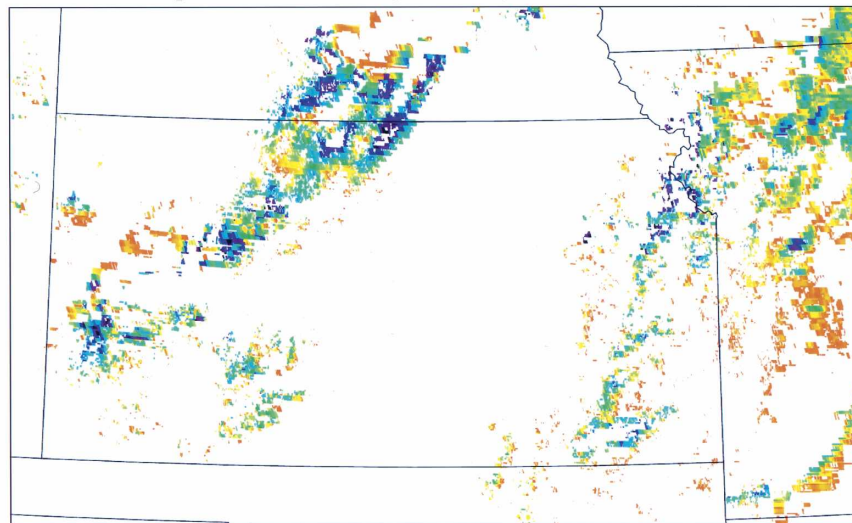-50   -40   -30   -20   -10   0
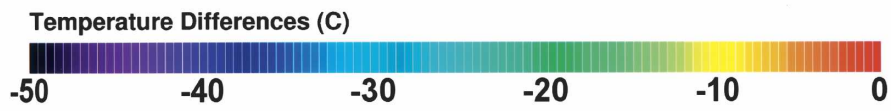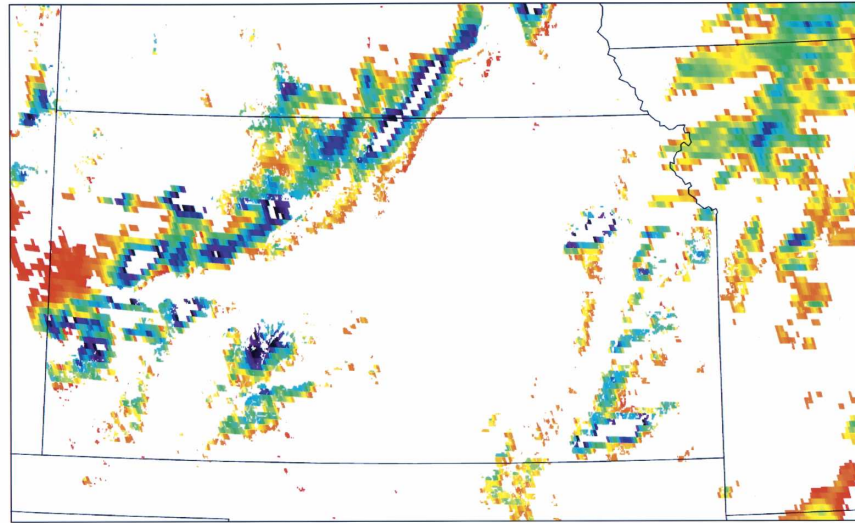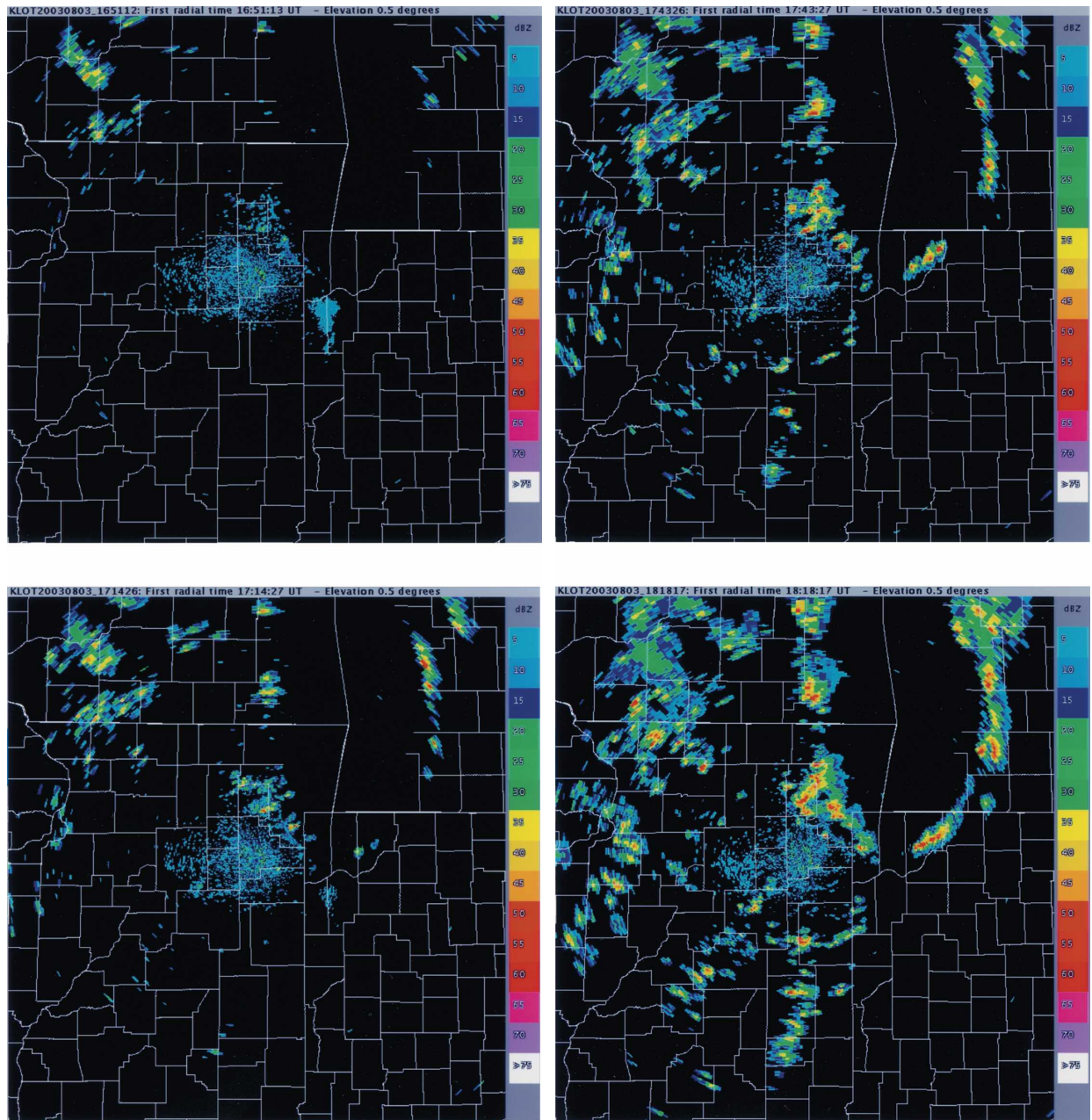
FIG. 14. (*Continued*)

FIG. 15. NEXRAD WSR-88D base reflectivity from KLOT at (a) 1645, (b) 1715, (c) 1745, and (d) 1815 UTC on 3 Aug 2003.

channel differencing techniques to identify cumulus in a pre-CI state, and finally by utilizing combined VIS and IR satellite-derived AMVs as a means of tracking individual cumulus clouds in sequential imagery to estimate cloud-top trends. In effect, these techniques isolate only the cumulus convection in satellite imagery, track moving cumulus convection, and monitor their IR cloud properties in time. Convective initiation is predicted through the accumulation of information within a satellite pixel that is attributed to the first occurrence of a

≥ 35 dBZ radar echo as obtained from WSR-88D mosaic data.

Given the satellite tracking of moving cumulus for the monitoring of CI, this work represents an advance in the ability to predict CI in routinely available, real-time data streams. The processing methods presented are fully capable of operating in real time (≤ 15 min computational time using a single ~2 GHz Pentium IV computer running the Linux operating system) over large geographical regions [$\mathbf{O}(10^6)$ 1-km pixels], or

Satellite data valid at: 1715 UTC 3 August 2003
Nowcast for Future CI (red), Cirrus and Mature Cu (grey)
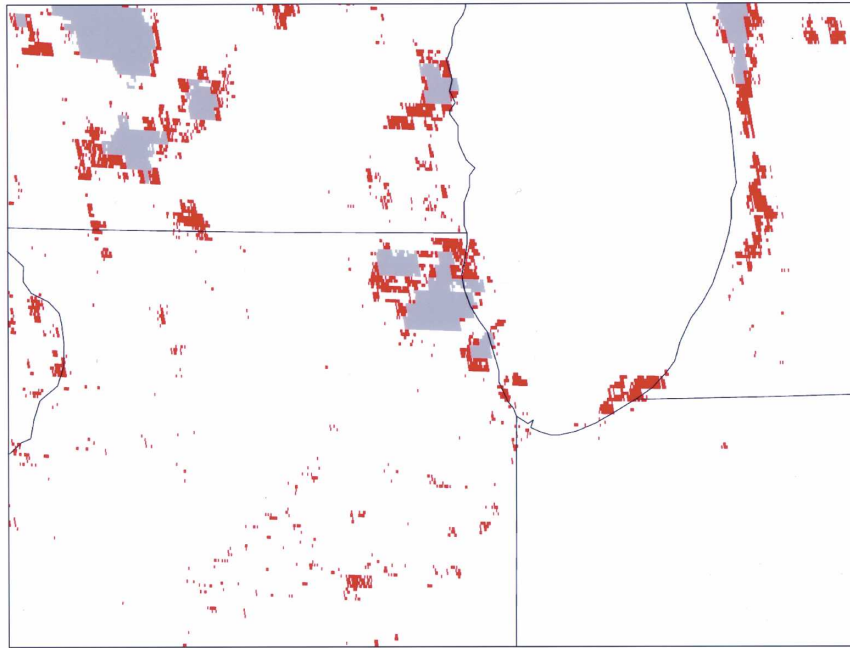
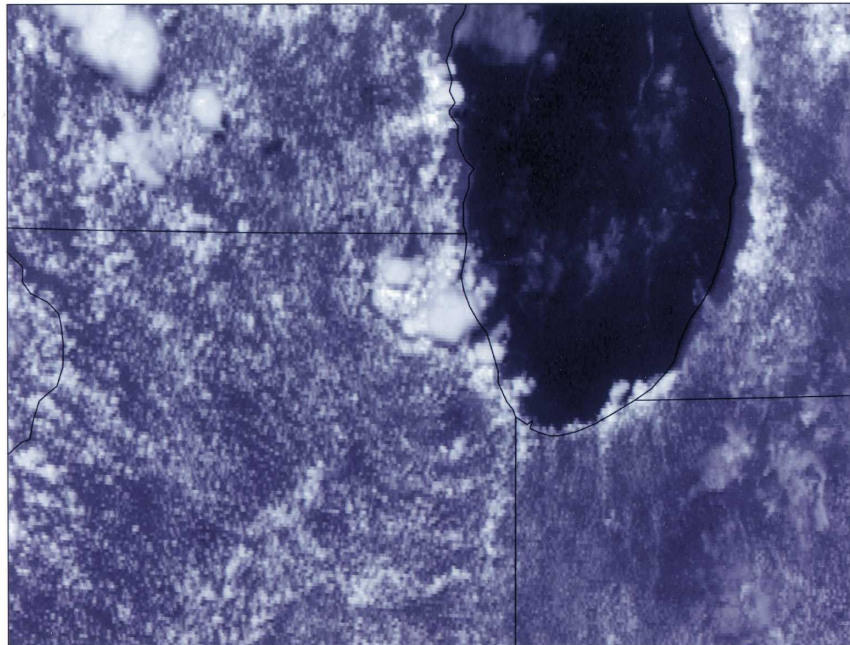## Satellite data valid at: 1715 UTC 3 August 2003
Visible Brightness

FIG. 16. (a) The CI nowcast product, and (b) the *GOES-12* 1-km visible satellite image, valid at 1715 UTC on 3 Aug 2003.
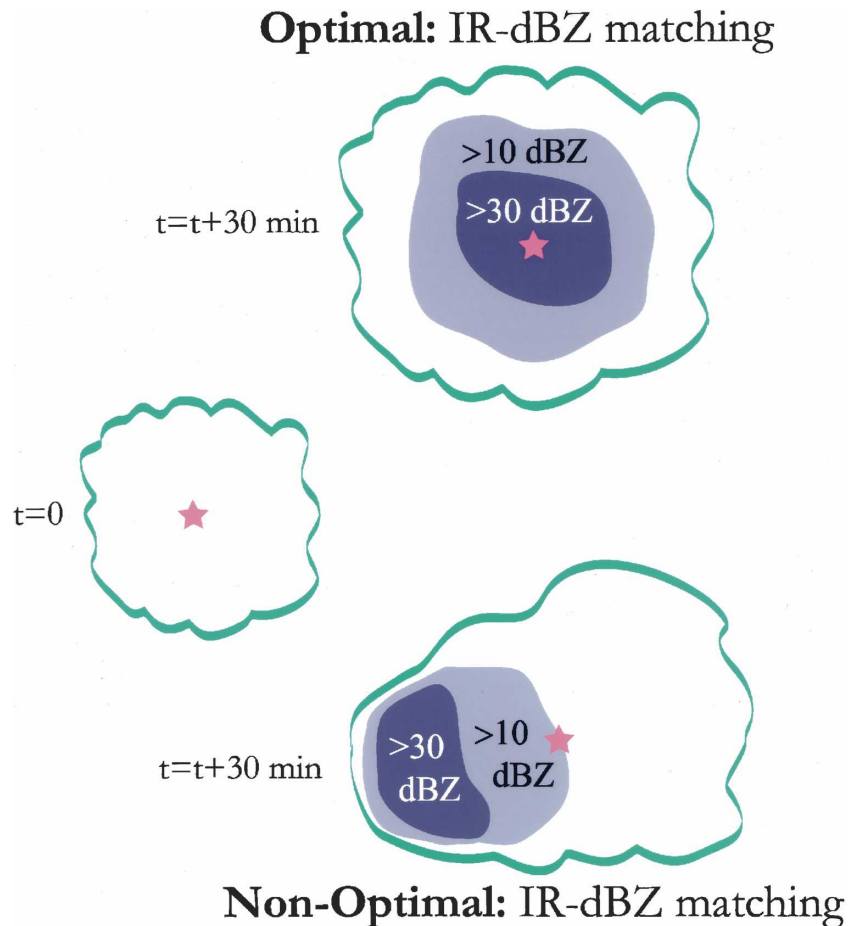
Optimal: IR-dBZ matching

FIG. 17. Schematic that demonstrates the problems associated with correlating a radar echo with a satellite-viewed cloud in the IR portion of the spectrum. The left diagram shows the initial size and shape of a cumulus at the time of a CI nowcast ($t = 0$). The star represents a pixel where at least seven CI interest field criteria are met (i.e., a CI nowcast pixel). In upper-right diagram ("Optimal"), the radar echo (dBZ) maximum corresponds well with the cloud-relative location of the CI nowcast pixel 30 min later. This correspondence results from relatively low vertical shear and simplistic internal cumulus dynamics, similar to that found in a summertime "airmass" thunderstorm over the southern United States. In the lower-right diagram ("Non-optimal"), the CI nowcast pixel and radar echoes are poorly related in space. This results from high vertical shear and complex internal cumulus dynamics, causing the precipitation to shift away from the cloud-relative location of satellite-derived CI signatures (i.e., center of the cloud). This situation can occur in association with a squall line or supercell-type thunderstorm and leads to "error" within the methods described, despite the fact that our methods have "nowcasted" the presence of a precipitating cumulus cloud at a 30-min lead time in both cases.

about one-fourth–one-third of the continental United States. The large-scale processing as part of this algorithm is made possible through use of a cumulus mask that isolates only the 10%–30% of convective clouds within a GOES VIS image.

This research represents a logical next step in the study of convective storms with satellite imagery. In addition to adopting and incorporating results from other research, this study is unique in its first use of several IR multispectral methods for monitoring convective clouds, namely, the 13.3–10.7 μm, ∂[6.5 (or 6.7)–10.7 μm]/∂t, and ∂[13.3 (or 12)–10.7μm]/∂t interest fields, as well as for tracking convective clouds in successive satellite images using GOES-derived AMVs for monitoring convective cloud trends. Use of AMVs in this context, *especially those that contain information on the nongeostrophically balanced portion of the flow*, has not been a primary motivation in other satellite-wind

studies to date [exceptions being Rabin (2002) and Rabin et al. (2004)]. Hence, for this study the VIS and IR AMVs contain both balanced and divergent flow components due to modifications made to the AMV processing algorithm. Once cumulus cloud tracking is established using SOVs, six IR properties (creating eight interest fields) of the clouds are monitored at 1-km resolution for their relative importance with respect to CI occurrence. The method achieves ~60%–70% accuracy when applied to three case events that comprise a range of synoptic and mesoscale forcing regimes.

Algorithm adjustments are likely needed before this method may be applied over environments that differ significantly from those presented here (i.e., midlatitude), over the Tropics in particular, where "warm rain" microphysical processes play a large role in rainfall initiation. Another area of active work is toward operating this algorithm at night when the convective cloud mask (in its present form) cannot be used, 3.9-μm AMVs replace VIS AMVs, and we are limited to 4-km IR resolution data. This new research will be reported on in subsequent papers.

REFERENCES

Ackerman, S. A., 1996: Global satellite observations of negative brightness temperature differences between 11 and 6.7 μm. *J. Atmos. Sci.,* **53,** 2803–2812.

Adler, R. F., and D. D. Fenn, 1979: Thunderstorm vertical velocity estimated from satellite data. *J. Atmos. Sci.,* **36,** 1747–1754.

——, M. J. Markus, and D. D. Feen, 1985: Detection of severe Midwest thunderstorms using geosynchronous satellite data. *Mon. Wea. Rev.,* **113,** 769–781.

Bankert, R. L., 1994: Cloud classification of AVHRR imagery in maritime regions using a probabilistic neural network. *J. Appl. Meteor.,* **33,** 909–918.

Barnes, S. L., 1964: A technique for maximizing details in numerical weather map analysis. *J. Appl. Meteor.,* **3,** 396–409.

Baum, B. A., V. Tovinkere, J. Titlow, and R. M. Welch, 1997: Automated cloud classification of global AVHRR data using a fuzzy logic approach. *J. Appl. Meteor.,* **36,** 1519–1540.

Beckman, S. K., 1986: Relationship between cloud bands in satellite imagery and severe weather. *Satellite Imagery Interpretation for Forecasters,* Vol. 2, *Precipitation Convection,* P. S. Parke, Ed., National Weather Association. [Available from the NWA, 4400 Stamp Road, No. 404, Temple Hills, MD 20748.]

Bedka, K. M., and J. R. Mecikalski, 2005: Application of satellite-derived atmospheric vectors for estimating mesoscale flows. *J. Appl. Meteor.,* **44,** 1761–1772.

Ellrod, G. P., 1995: Advances in the detection and analysis of fog at night using GOES multispectral infrared imagery. *Wea. Forecasting,* **10,** 606–619.

——, 2004: Loss of the 12 μm "Split Window" band on GOES-M: Impacts on volcanic ash detection. *J. Volc. Geothermal Res.,* **135** (1–2), 91–103.

Fujita, T. T., E. W. Fearl, and W. E. Shenk, 1975: Satellite-tracked cumulus velocities. *J. Appl. Meteor.,* **14,** 407–413.

Griffith, C. G., W. L. Woodley, P. G. Grube, D. W. Martin, J. Stout, and D. N. Sikdar, 1978: Rain estimation from geosynchronous imagery—Visible and infrared studies. *Mon. Wea. Rev.,* **106,** 1153–1171.

Hand, W. H., 1996: An object-oriented technique for nowcasting heavy showers and thunderstorms. *Meteor. Appl.,* **3,** 31–41.

Hayden, C. M., G. S. Wade, and T. J. Schmit, 1996: Derived product imagery from GOES-8. *J. Appl. Meteor.,* **35,** 153–162.

Hill, J., 1991: *Weather from Above: America's Meteorological Satellites.* Smithsonian Institution Press, 89 pp.

Inoue, T., 1987: An instantaneous delineation of convective rainfall area using split window data of NOAA-7 AVHRR. *J. Meteor. Soc. Japan,* **65,** 469–481.

Kuo, K. S., R. M. Welch, and R. C. Weger, 1993: The three-dimensional structure of cumulus clouds over the ocean. 1. Structural analysis. *J. Geophys. Res.,* **98,** 20 685–20 711.

Levizzani, V., and M. Setvák, 1996: Multispectral, high-resolution satellite observations of plumes on top of convective storms. *J. Atmos. Sci.,* **53,** 361–369.

Markowski, P., C. Hannon, and E. Rasmussen, 2006: Observations of convection initiation "failure" from the 12 June 2002 IHOP deployment. *Mon. Wea. Rev.,* **134,** 375–405.

Mecikalski, J. R., D. B. Johnson, J. J. Murray, and many others at UW-CIMSS and NCAR, 2002: NASA Advanced Satellite Aviation-weather Products (ASAP) study report. NASA Tech. Rep., 65 pp. [Available from the Schwerdtferger Library, 1225 West Dayton Street, University of Wisconsin—Madison, Madison, WI 53706.]

Medlin, J. M., and P. J. Croft, 1998: A preliminary investigation and diagnosis of weak shear summertime convective initiation for extreme southwest Alabama. *Wea. Forecasting,* **13,** 717–728.

Menzel, W. P., and J. F. W. Purdom, 1994: Introducing GOES-I: The first of a new generation of geostationary operational environmental satellites. *Bull. Amer. Meteor. Soc.,* **75,** 757–781.

——, F. C. Holt, T. J. Schmit, R. M. Aune, A. J. Schreiner, and D. G. Gray, 1998: Application of *GOES-8/9* soundings to weather forecasting and nowcasting. *Bull. Amer. Meteor. Soc.,* **79,** 2059–2077.

McCann, D. W., 1983: The enhanced-V: A satellite observable severe storm signature. *Mon. Wea. Rev.,* **111,** 887–894.

Minnis, P., and D. F. Young, 2000: Cloud microphysical properties derived from geostationary satellite data. *Proc. EUMETSAT Meteorological Satellite Data Users' Conf. 2000,* Bologna, Italy, EUMETSAT, 299–305.

Mueller, C. K., J. W. Wilson, and N. A. Crook, 1993: The utility of sounding and mesonet data to nowcast thunderstorm initiation. *Wea. Forecasting,* **8,** 132–146.

——, T. Saxen, R. Roberts, J. Wilson, T. Betancourt, S. Dettling, N. Oien, and J. Yee, 2003: NCAR Auto-Nowcast system. *Wea. Forecasting,* **18,** 545–561.

Murray, J. J., 2002: Aviation weather applications of Earth Science Enterprise data. *Earth Observation Magazine,* Vol. 11, No. 8, GITC America, 27–30.

Nair, U. S., R. C. Weger, K. S. Kuo, and R. M. Welch, 1998: Clustering, randomness, and regularity in cloud fields. 5. The nature of regular cumulus cloud fields. *J. Geophys. Res.,* **103,** 11 363–11 380.

——, J. A. Rushing, R. Ramachadran, K. S. Kuo, R. M. Welch, and S. J. Graves, 1999: Detection of cumulus cloud fields in satellite imagery. *Proc. SPIE Conf. on Earth Observing Systems IV,* Denver, CO, SPIE, 345–355.

Parke, P. S., Ed., 1986: *Satellite Imagery Interpretation for Forecasters.* Vol. 2, *Precipitation Convection,* National Weather Association. [Available from the NWA, 4400 Stamp Road, No. 404, Temple Hills, MD 20748.]

Prata, A. J., 1989: Observations of volcanic ash clouds in the 10–12 μm window using AVHRR/2 data. *Int. J. Remote Sens.,* **10,** 751–761.

Purdom, J. F. W., 1976: Some uses of high resolution GOES imagery in the mesoscale forecasting of convection and its behavior. *Mon. Wea. Rev.,* **104,** 1474–1483.

——, 1982: Subjective interpretations of geostationary satellite data for nowcasting. *Nowcasting,* K. Browning, Ed., Academic Press, 149–166.

——, 1986: The development and evolution of deep convection. *Satellite Imagery Interpretation for Forecasters.* Vol. 2, *Precipitation Convection,* P. S. Parke, Ed., National Weather Association, 4-a-1–4-a-8. [Available from the NWA, 4400 Stamp Road, No. 404, Temple Hills, MD, 20748.]

Rabin, R. M., 2002: Mesoscale winds in vicinity of convection and winter storms, *Proc. Sixth Int. Winds Workshop,* Madison, WI, EUMETSAT, 89–96.

——, S. F. Corfidi, J. C. Brunner, and C. E. Hain, 2004: Detecting winds aloft from water vapour satellite imagery in the vicinity of storms. *Weather,* **59,** 251–257.

Riehl, H., and R. A. Schleusener, 1962: On identification of hail-bearing clouds from satellite photographs. Atmospheric Science Tech. Paper 27, Department of Atmospheric Science, Colorado State University, 7 pp.

Roberts, R. D., and S. Rutledge, 2003: Nowcasting storm initiation and growth using *GOES-8* and WSR-88D data. *Wea. Forecasting,* **18,** 562–584.

Roohr, P. B., and T. H. Vonder Haar, 1994: A comparative analysis of temporal variability of lightning observations and GOES imagery. *J. Appl. Meteor.,* **33,** 1271–1290.

Schmetz, J., S. A. Tjemkes, M. Gube, and L. van de Berg, 1997: Monitoring deep convection and convective overshooting with METEOSAT. *Adv. Space Res.,* **19,** 433–441.

Schmit, T. J., W. F. Feltz, W. P. Menzel, J. Jung, A. P. Noel, J. N. Heil, J. P. Nelsen, and G. S. Wade, 2002: Validation and use of GOES sounder moisture information. *Wea. Forecasting,* **17,** 139–154.

Schreiner, A. T., T. J. Schmit, and W. P. Menzel, 2001: Observed trends of clouds based on GOES sounder data. *J. Geophys. Res.,* **106,** 20 349–20 363.

Setvák, M., and C. A. Doswell III, 1991: The AVHRR channel 3 cloud top reflectivity of convective storms. *Mon. Wea. Rev.,* **119,** 841–847.

——, R. M. Rabin, C. A. Doswell III, and V. Levizzani, 2003: Satellite observations of convective storm top features in the 1.6 and 3.7/3.9 μm spectral bands. *Atmos. Res.,* **67–68C,** 589–605.

Soden, B., and F. P. Bretherton, 1993: Upper tropospheric humidity from GOES 6.7 μm channel: Method and climatology for July 1987. *J. Geophys. Res.,* **98,** 16 669–16 688.

Strabala, K. I., S. A. Ackerman, and W. P. Menzel, 1994: Cloud properties inferred from 8–12 μm data. *J. Appl. Meteor.,* **33,** 212–229.

Uddstrom, M. J., and W. R. Gray, 1996: Satellite cloud classification and rain-rate estimation using multispectral radiances and measures of spatial texture. *J. Appl. Meteor.,* **35,** 839–858.

Velden, C. S., C. M. Hayden, S. J. Nieman, W. P. Menzel, S. Wanzong, and J. S. Goerss, 1997: Upper-tropospheric winds derived from geostationary satellite water vapor observations. *Bull. Amer. Meteor. Soc.,* **78,** 173–195.

——, T. Olander, and S. Wanzong, 1998: The impact of multispectral GOES-8 wind information on Atlantic tropical cyclone track forecasts in 1995. Part I: Dataset methodology, description, and case analysis. *Mon. Wea. Rev.,* **126,** 1202–1218.

Weckwerth, T. M., and D. B. Parsons, 2006: A review of convective initiation and motivation for IHOP_2002. *Mon. Wea. Rev.,* **134,** 5–22.

——, and Coauthors, 2004: An overview of the International H$_2$O Project (IHOP_2002) and some preliminary highlights. *Bull. Amer. Meteor. Soc.,* **85,** 253–277.

Weldon, R. B., and S. J. Holmes, 1991: Water vapor imagery: Interpretation and applications to weather analysis and forecasting. NOAA Tech. Rep. NESDIS 57, U.S. Dept. of Commerce, 213 pp.

Wielicki, B. A., and R. M. Welch, 1986: Cumulus cloud properties derived using Landsat satellite data. *J. Appl. Meteor.,* **25,** 261–276.